
CMS Draft Analysis Note

The content of this note is intended for CMS internal use and distribution only

2010/02/13

Head Id: 2682

Archive Id: 2821:2827

Archive Date: 2010/02/11

Archive Tag: trunk

Measurement of the charge asymmetry of atmospheric muons with the CMS detector

M. Aldaya¹, A. Calderon², A. Fanfani³, I. K. Furić⁴, P. Garcia-Abia⁵, U. Gasparini⁶, A. Gresele⁷, G. Hesketh⁸, T. N. Kypreos⁴, S. Marcellini³, M. Mulders⁸, J. Piedra⁴, and L. Sonnenschein⁹

¹ DESY, Hamburg, Germany

² Instituto de Física de Cantabria, Spain

³ University and INFN Bologna, Italy

⁴ University of Florida, USA

⁵ CIEMAT, Madrid, Spain

⁶ University and INFN Padova, Italy

⁷ INFN Trento, Italy

⁸ CERN, Geneva, Switzerland

⁹ RWTH Aachen, Germany

Abstract

This note presents the measurement of the ratio of positive- to negative-charge muons from cosmic ray interactions in the atmosphere, performed as a function of the vertical component of the muon momentum, using data collected by the CMS experiment at the *Magnet Test and Cosmic Challenge* (2006) and at the *Cosmic Run At Four Tesla* (2008). These cosmic runs are important commissioning milestones in the CMS detector construction and operation, and provide high quality data used in this analysis. The excellent performance of the CMS detector allowed detection of muons from 3 GeV/c to 1 TeV/c and yielded the most precise measurement to date of the atmospheric muon charge asymmetry in much of the accessible momentum range. This is the first measurement of a physical quantity performed with muons by the CMS experiment.

This box is only visible in draft mode. Please make sure the values below make sense.

PDFAuthor: M. Aldaya, A. Calderon, A. Fanfani, I. K. Furic, P. Garcia-Abia, U. Gasparini, A. Gresele, G. Hesketh, T. N. Kypreos, S. Marcellini, M. Mulders, J. Piedra, L. Sonnenschein
PDFTitle: Measurement of the charge asymmetry of atmospheric muons with the CMS detector
PDFSubject: CMS
PDFKeywords: CMS, physics, muon, cosmics, charge ratio

Please also verify that the abstract does not use any user defined symbols

DRAFT

1 Introduction

The *Compact Muon Solenoid* (CMS) [1] is one of the four detectors installed at the *Large Hadron Collider* (LHC) [2] at CERN (Geneva, Switzerland). The CMS experiment will search for signals of new physics in the high energy frontier, collecting and analyzing data from proton-proton (pp) collisions at center of mass energies up to 14 TeV [3].

The CMS detector is installed in an underground cavern, with the center of the detector 89 metres below the Earth surface. A large, four-Tesla, superconducting solenoid magnet hosts a high precision tracking system enclosed in electromagnetic and hadron calorimeters. Outside the magnet, a large muon detector is interleaved with the steel absorber plates that act as the return yoke of the magnet. Given the high complexity of the detector, it is essential to test and verify all its components at every step of the construction and assembly procedure, in order to ensure the optimal functioning of CMS at startup.

Crucial milestones in the commissioning of CMS were the *cosmics runs*, major data-taking campaigns devoted to test the detector: magnet, readout electronics, trigger and data acquisition system (DAQ), alignment, calibration and event reconstruction algorithms. High energy muons from cosmic rays are used as a particle beam for these tests. While physics studies were not among the primary goals of the cosmics runs, these tests provided high quality data that can be used to perform measurements of physical quantities related to cosmic muons.

The *muon charge ratio*, R , is defined as the ratio of the number of positive- to negative-charge cosmic muons. Atmospheric muons stem from cosmic ray showers, produced via interactions of high-energy cosmic-ray particles, entering the upper layers of the atmosphere, with air nuclei: $(p, \text{He}, \dots, \text{Fe}) + A \rightarrow \text{hadrons}, e^\pm \gamma$, where $(\pi^\pm, K^\pm) \rightarrow \mu^\pm + \nu_\mu (\bar{\nu}_\mu)$ and $\mu^\pm \rightarrow e^\pm + \bar{\nu}_\mu (\nu_\mu) + \nu_e (\bar{\nu}_e)$. The charge and momentum dependence of R is determined by the meson production cross sections in these high-energy hadronic interactions. As both cosmic rays and air are mainly protons and nuclei, positive meson production is favored, hence more positive muons are expected. Previous measurements from various experiments [4, 5] show the muon charge ratio to be constant up to a momentum scale of about 500 GeV/c, significantly increasing above this value due to the additional contribution of muons from kaon decays. These measurements are used to constrain parameters relevant to low energy hadronic interactions and to better determine the atmospheric neutrino flux.

This note presents the measurement of the muon charge ratio using CMS data, collected at two major cosmics runs. The analysis is performed using the standard CMS reconstruction software, and the same data distribution and job submission Grid tools used for the analysis of the CMS data produced in pp collisions at the LHC.

2 Experimental setup, data samples, and event simulation

The interaction point of CMS is located at $46^\circ 18.5667'$ north latitude and $6^\circ 4.6167'$ east longitude, at an elevation of 420.13 m above sea level (89 m below the Earth surface). The upper 50 m of the earth above CMS consist of moraines, followed by molasse rock. A large access shaft with a diameter of 20.5 m rises vertically to the surface, and is offset from the center of CMS by 14 m, as illustrated in Fig. 1. It is covered by a 2.25 m thick concrete plug. Thus, depending on the point of impact on CMS, the overburden for close-to-vertical muons varies from approximately 6 to 175 meters of water equivalent.

CMS uses a right-handed coordinate system, with the origin at the nominal proton-proton collision point, the x -axis pointing to the center of the LHC, the y -axis pointing up (perpendicular

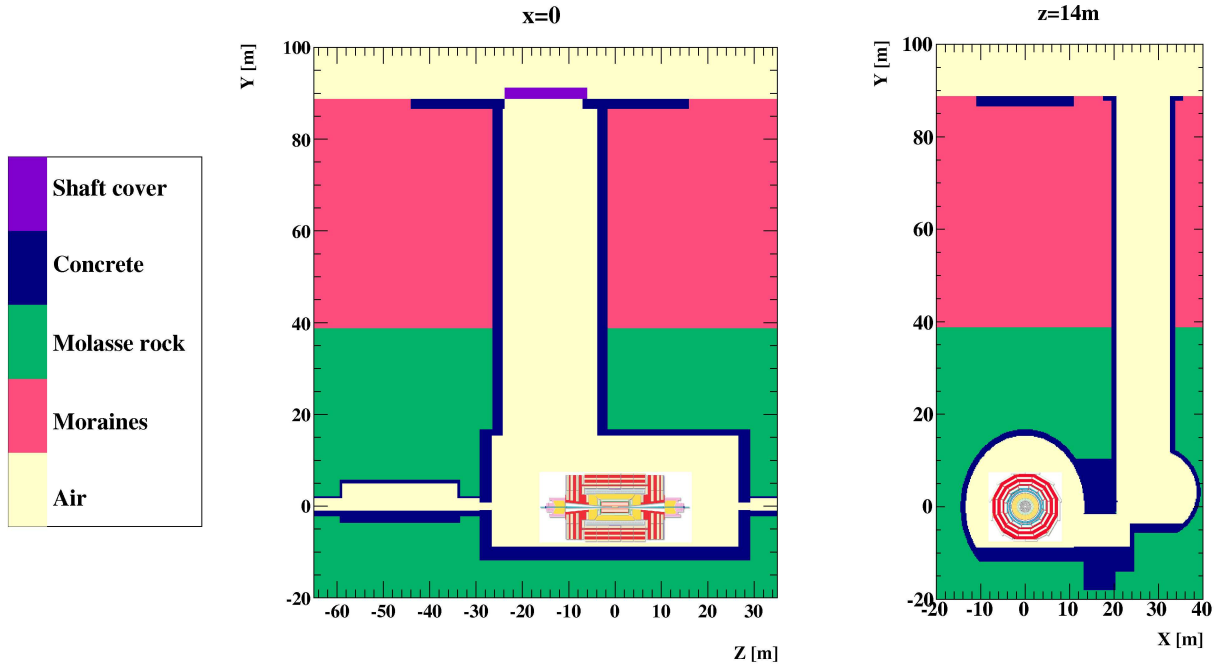


Figure 1: Description of geometry and different materials of the CMS infrastructure and surrounding geological layers.

45 to the LHC plane), and the z -axis along the anticlockwise-beam direction, at 280.2° of the ge-
 46 ographic azimuth. The polar angle, θ , is measured from the positive z -axis and the azimuthal
 47 angle, ϕ , is measured in the x - y plane. The gradient of the LHC beam axis at this point is -
 48 12.34 mrad (1.2%) and the gradient to the centre of the LHC machine is -7.93 mrad (0.8%). Thus
 49 the angle between the CMS y -axis and the local Zenith direction is 0.8° . This small difference is
 50 negligible (and therefore neglected) in the analyses reported here.

51 2.1 Data samples

52 CMS performed three major cosmics runs in the last three years of the detector construction and
 53 commissioning phase: the *Magnet Test and Cosmic Challenge* (MTCC, 2006) [6] and the *Cosmic*
 54 *Run At Four Tesla* (CRAFT08, 2008) [7]. Data from the most recent run (CRAFT09, 2009) is not
 55 used in the analysis reported here.

56 In August 2006 the CMS detector was pre-assembled in the surface hall before being lowered to
 57 the cavern. A small fraction of each of the sub-detectors was installed and available at the time.
 58 The details of the MTCC setup are described elsewhere [6, 8]. About 25 million good quality
 59 cosmic muon events were recorded during the first phase of the MTCC with the magnet at a
 60 field strength between 3.67 T and 4.0 T.

61 CRAFT08 was a month-long sustained data-taking exercise with the CMS detector fully as-
 62 sembled in its final position underground. The full detector, ready for collecting collision data
 63 delivered by LHC and magnet on at the nominal field of 3.8 T, participated in the run, which
 64 took place in October and November 2008. Approximately 270 million cosmic muon events
 65 were recorded.

2.2 Simulation of cosmic muons

The analyses presented here rely only minimally on Monte Carlo simulation. In two of the three analyses simulation is used to derive corrections for detector resolution effects. The third analysis does not use simulation at all to obtain the central result. Simulated events are used, however, to cross check efficiencies, demonstrate the validity of data-based methods applied, and to study possible systematic effects.

Cosmic muons are simulated by means of the Monte-Carlo event generator CMSCGEN [9][10], which makes use of parameterizations of the muon energy and incidence angle. These parameterizations are based both on measured and simulated data of the cosmic muon flux as a function of the muon energy and incidence angle obtained by means of the air shower program CORSIKA [11].

The simulated muons are propagated through a material map [10] from surface to the CMS detector to obtain an integrated amount of water equivalents. This determines the average expected energy loss of a given muon as function of the energy and direction of the incident muon at surface [12]. The material map describes the various materials from the Earth surface to the CMS detector. The model takes into account the foundation of the hall at surface, the three vertical access shafts, a movable shaft cover of the main shaft (in re-inforced concrete) as well as the collision and service caverns, including the adjacent parts of the LHC tunnel. Two different average densities of moraines and molasses rock are assigned to the geological layers surrounding the CMS infrastructure. In Fig. 1 the geometry and different materials are shown as implemented in the simulation.

Exactly the same code is used (cf. section 4) to extrapolate each cosmic muon measured in CMS back to the Earth surface, correcting for the expected energy loss on a per-muon basis.

3 Analysis and event selection

Muons are reconstructed in CMS combining signals from different sub-detectors, the most crucial ones being the muon chambers, the silicon tracker and the pixel detector. Figure 2 displays a cosmic muon crossing the CMS detector from top to bottom, recorded in CRAFT08. Cosmic muons cross CMS at random times and at random distances from the nominal center of CMS, the proton-proton interaction point. The very good spatial resolution of the silicon tracker provides a high quality measurement of the muon momentum. Muons not traversing the silicon tracker are reconstructed using the information extracted from the muon chambers alone, a sub-detector with large geometrical acceptance but a lower spatial resolution.

Two independent analyses exploit these two sub-detectors in an almost orthogonal manner, yielding results mostly uncorrelated from the tracking point of view. One, designated as *global-muon analysis*, uses muons reconstructed both in the muon detector and in the silicon tracker. The other analysis, referred to as *standalone-muon analysis*, uses cosmic muons reconstructed from the signals of the muon chambers alone, regardless of the presence of signals in the silicon tracker.

The global-muon analysis deals with a smaller number of events, limited by the acceptance of the silicon tracker, but with very good momentum resolution.

The standalone-muon analysis profits from the larger size of the muon chambers yielding an enriched sample of muons (about 20 times larger), at the price of a lower momentum resolution. Still, by performing a track fit including muon hits in both top and bottom halves of the

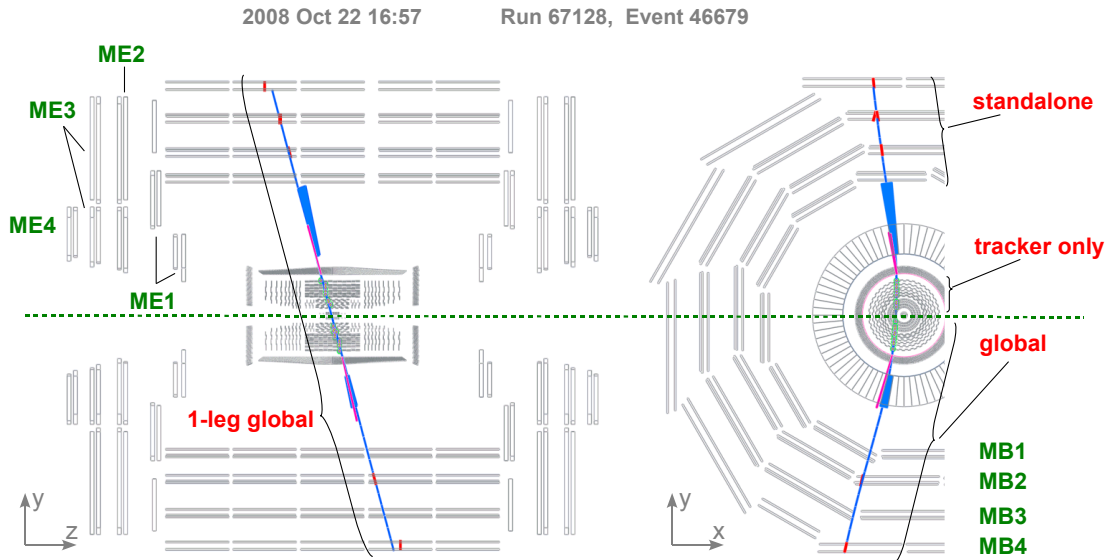


Figure 2: Cosmic muon crossing the CMS detector from top to bottom, recorded in CRAFT08, leaving signals in the muon system, tracking detectors and calorimeters.

109 detector, profiting from the long bending arm in the strong central magnetic field, a reliable
 110 charge and momentum determination up to the TeV range can be achieved.

111 A third analysis, based on MTCC data [8], also uses standalone muons. The reduced detector
 112 setup used at MTCC, having just a fraction of the bottom half of the muon detector, resulted
 113 in short muon tracks with a significantly worse momentum resolution. Having the detector on
 114 surface, however, permitted collecting a large number of low momentum muons, down to a
 115 vertical component of the momentum of ~ 3 GeV/c, allowing for a precise measurement of the
 116 charge ratio in the low momentum range.

117 3.1 CRAFT08: global-muon analysis

118 The key feature of this analysis is the choice to reconstruct two halves of each cosmic muon
 119 independently, and to use the differences in reconstructed parameters between the top and
 120 bottom halves to obtain a fully data driven handle on momentum resolution and charge mis-
 121 assignment.

122 To achieve good tracking resolution even with half the CMS detector, two independent track
 123 segments of good quality are reconstructed from a sufficient number of layers in the silicon
 124 tracker. Effectively, this choice limits the acceptance to muons with an impact parameter less
 125 than 30-40 cm from the nominal center of CMS.

The detector is formally split along the horizontal axis into a “top” half-cylinder ($y > 0$) and a “bottom” one ($y < 0$). Muons passing through the detector leave hits in the “top” and “bottom” muon half-cylinders. The muon trajectory is reconstructed twice in the tracker system, in both the top and the bottom halves of the detector. The tracker and muon system information which belong to the same half are combined to obtain two independent muon trajectories, top and bottom. Their corresponding transverse momentum (p_T) measurements of the two are

combined by means of a simple average,

$$\left(\frac{q}{p_T}\right)_{combined} = \frac{1}{2} \left[\left(\frac{q}{p_T}\right)_{top} + \left(\frac{q}{p_T}\right)_{bottom} \right]; \quad d_C = \frac{1}{2} \left[\left(\frac{q}{p_T}\right)_{top} - \left(\frac{q}{p_T}\right)_{bottom} \right], \quad (1)$$

126 where q denotes the muon charge, $p_{T,combined}$ is the combined transverse momentum, and $p_{T,top}$
 127 and $p_{T,bottom}$ are the top and bottom transverse momenta, respectively. The distribution of
 128 the half-difference, d_C , provides an excellent data-driven measurement of the resolution of the
 129 $p_{T,combined}$ momentum measurement. We have tested this assumption on toy Monte Carlo en-
 130 sembles with Gaussian and exponential resolution functions, as well as on full simulated events
 131 (Fig. 3). Both the core resolution and tails are well reproduced. Measurements of the other four
 132 trajectory parameters are also combined in this way to obtain resolution estimates for the po-
 133 lar angle of the momentum with respect to the beam axis ($\cot\theta$), the azimuthal angle in the
 134 plane transverse to the beam axis (ϕ_0), the transverse distance (d_0) and z coordinate (z_0) of
 135 the *point of closest approach* (PCA) to the nominal LHC beam line. The unweighted average of
 136 two measurements, Eq. 1, is not the optimal combination in terms of resolution, but has the
 137 crucial advantage that it provides a well-defined data-driven estimate of the resolution func-
 138 tion, allowing this analysis not to rely on the simulation studies. The key points at which the
 139 data-driven resolution function, d_C , is utilized are the derivation of the momentum resolution
 matrix and establishing event quality requirements.

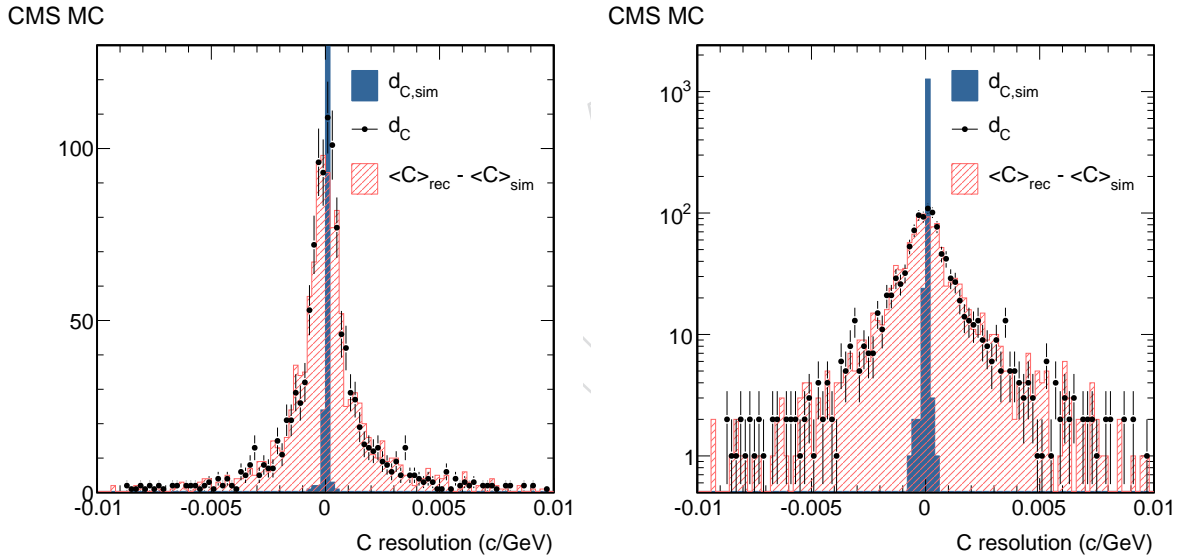


Figure 3: Comparison of the (q/p_T) resolution proxy d_C (black points) with the true curvature resolution δC (hashed red histogram), both in (left) linear and (right) logarithmic scales. The simulation jitter $d_{C,sim}$ (solid blue histogram) indicates the indetermination of the 'true' resolution in MC, due to the fact that this information is not stored at PCA for simulated cosmic muons, but extracted from the *simulated hits* closest to PCA.

140

141 Quality requirements are selected to simultaneously ensure homogeneous properties of the
 142 data analyzed and high efficiency. Using split tracks, the momentum resolution, charge mis-
 143 assignment probability and efficiency are determined for different selection requirements. The
 144 working point is chosen by requiring the highest efficiency at which the resolution and charge
 145 mis-assignment distributions flatten out. The procedure involves a judgment call on our side

146 as to where the requirement is placed, but is unbiased with respect to the outcome of the charge
 147 ratio measurement. As an example, one can see the procedure for the number of hits in the drift
 tubes muon system (DT) in Fig. 4.

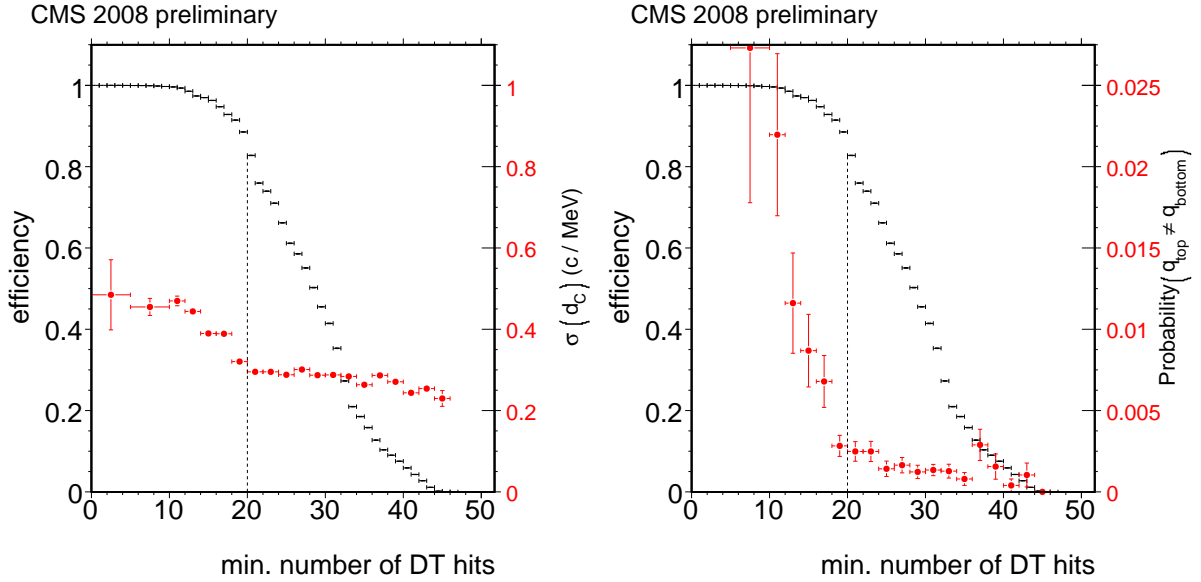


Figure 4: (Left) Efficiency and d_C vs. minimum number of DT hits. (Right) Efficiency and charge confusion vs. minimum number of DT hits.

148

149 In order to achieve a good fit of the muon trajectory in the tracker, we require that the muon
 150 trajectory contains at least 5 hits in the tracker outer barrel (TOB) system. In order to ensure a
 151 good fit in the muon chambers, we require at least 20 hits in the drift tubes system be present
 152 in the trajectory. Of these 20 hits, at least 3 have to be in superlayer 2 of a DT station. This
 153 ensures a good measurement of the polar angle, which is necessary to convert the transverse
 154 momentum into a full momentum measurement. The global-muon analysis focuses on barrel
 155 muons, thus we require that the muon trajectory contains no muon endcap (CSC) [13] hits or
 156 tracker endcap [14] hits. If the impact parameter of the cosmic track is too large, passing the
 157 silicon tracker too close to the edge, only a single good quality trajectory can be reconstructed
 158 in the tracker. We require that the two halves, top and bottom, of the same cosmic muon
 159 trajectory are reconstructed as two independent track segments in the silicon tracker. A loose
 160 cut is applied on the χ^2 of each of the two global-muon fits and we require that the polar angles
 161 match.

162 During CRAFT08 data taking, multiple triggers were utilized to collect the data. We analyze
 163 data gathered by the L1 single muon trigger. We remove noisy events and fake triggers (not
 164 from cosmic muons) by requiring the cosmic muon analyzed to be the one which fired the
 165 trigger. We enforce this by matching the trigger object and the reconstructed muon in ϕ at a
 166 radius $r = 5$ m from the center of the detector. A possible bias of the analysis due to trigger
 167 selection is described in Section 5.4.

168 The main background to this analysis comes from events in which multiple muon trajectories
 169 are present in the same event. In that case, there is a possibility that the two halves of a muon
 170 trajectory belong to different muons, yielding meaningless estimates of the muon momentum
 171 and resolution. We remove events with multiple muons with several requirements. We require
 172 exactly one standalone muon to be reconstructed in the top and exactly one muon in the bottom

173 of the detector. We require that the difference in η direction between the top and bottom global-
 174 muon trajectories be less than 0.2, and that the χ^2 of both global-muon trajectory fits be less
 175 than 1500. After all these requirements, no events are left in which multiple pairs of muons are
 176 reconstructed. Table 1 lists the selection requirements and compares the measured efficiency
 177 of each consecutive requirement between data and simulation. All selection requirements are
 178 symmetrically applied to the top and bottom muon trajectories. With the selected muons, we
 179 report some basic distributions in Figure 5. Finally, Figure 6 depicts the measured ratio of
 180 positive- to negative-charge cosmic muons at the PCA. Propagation of the muons to the Earth
 surface will be the next step, described in Section 4.

Table 1: Muon pairs passing the indicated selection requirements, and sequential selection efficiencies for the global-muon analysis. The efficiencies in simulation are shown as a reference, but they do not play a role in this analysis as it is fully data-driven. Differences are due to a momentum threshold at low momentum in the simulation, and known differences in the molasses model used in the MC samples leading to a differences in angular and momentum distributions.

selection	data			simulation		
	N	ϵ (%)	rel. ϵ (%)	N	ϵ (%)	rel. ϵ (%)
two silicon tracks	585794	24.7	24.7	92559	27.2	27.2
$N_{DT} \geq 20$	467116	19.7	79.7	80801	23.7	87.3
$N_{SL2 \in DT} \geq 3$	446267	18.8	95.5	78659	23.1	97.4
$N_{TOB} \geq 5$	431807	18.2	96.8	77859	22.8	99.0
$\Delta \cot \theta < 0.2$	431551	18.2	100.0	77825	22.8	100.0
$\max \chi^2 < 1500$	418390	17.6	97.0	75669	22.2	97.2
matched trigger	415173	17.5	99.2	75453	22.1	99.7
$p_T > 10 \text{ GeV}/c$	308390	13.0	74.3	57924	17.0	76.8

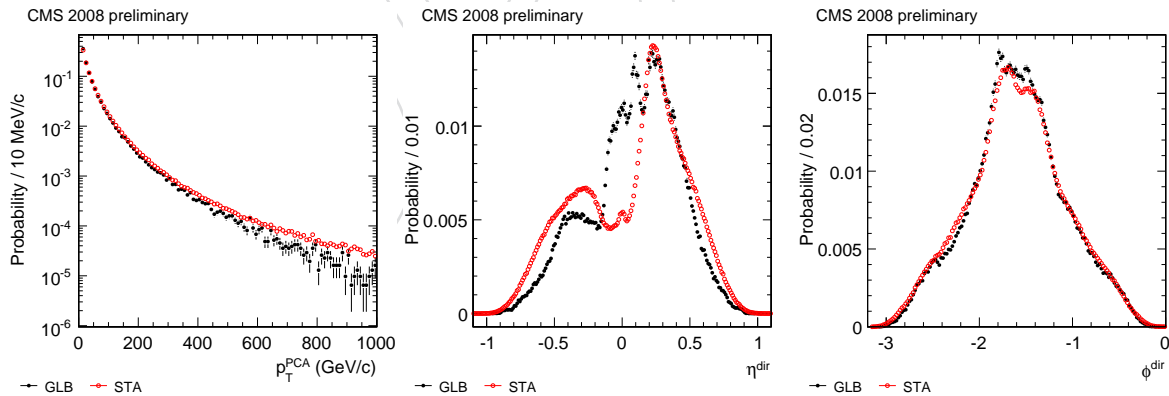


Figure 5: (Left) Muon p_T at the PCA. (Center) Muon direction η at the PCA. (Right) Muon direction ϕ at the PCA. Normalized distributions for the global- (GLB) and standalone-muon analysis (STA, cf. Section 3.2) are superimposed. As the standalone-muon analysis has a much larger impact parameter acceptance, the angular distributions are expected to be different.

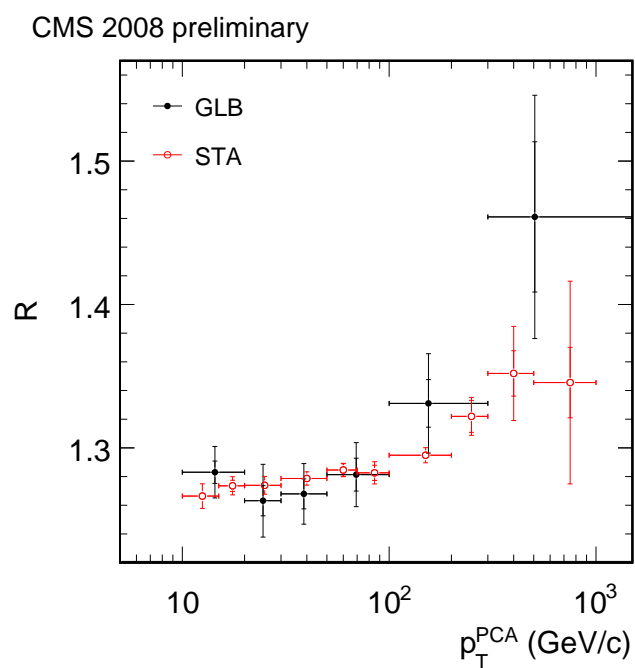


Figure 6: Charge ratio measured vs. p_T at the PCA, together with statistical and systematic error bars, for the global- (GLB) and standalone-muon analysis (STA, cf. Section 3.2)

3.2 CRAFT08: standalone-muon analysis

Rather than dividing cosmic muon tracks in top and bottom halves, this analysis obtains a data driven handle on momentum resolution and charge mis-assignment by comparing *standalone* tracks reconstructed in the muon system only, to independently reconstructed tracks in the silicon tracker. This is possible for about 1/3 of the selected standalone-muon events. Monte Carlo simulation is used to extrapolate the knowledge obtained from data to the other 2/3 of the sample.

The analysis is based on tracks reconstructed using only the information from the DT and RPC muon systems. Such tracks are called *standalone* muons [15]. Cosmic muon particles of sufficiently high momentum traverse the muon system through both the upper and the lower hemispheres. The particle trajectory is reconstructed using the DT and RPC muon hits from both hemispheres, providing a lever arm that allows a good momentum resolution also at high momenta. The same muon candidate can also be reconstructed as two split tracks, using the muon hits in the upper and lower part of CMS separately [15]. The *standalone*-muon analysis is based to the first type of track reconstruction. The tracks split in the upper and lower hemispheres are only used in the event selection requirements, as described below. The data used for the analysis are required to be collected in periods of stable DT operation, and the magnetic field had to be at the nominal value of 3.8 T.

The standalone-muon tracks, propagated through the CMS detector, are required to traverse the tracker region contained within a cylinder centered at the center of CMS, with a radius of 90 cm and a half-length of 130 cm. Only one standalone muon per event is allowed. The muon track is required to have a negative (ie downward pointing) azimuthal angle ϕ , defined at the *point of closest approach* (PCA) of the track with respect to the center of the CMS detector. To select muon tracks that are fully contained in the barrel region of the CMS detector, events with hits in the CSCs are rejected. To allow muon tracks to cross the whole CMS detector, muon candidates are required to have a reconstructed transverse momentum, measured at the PCA, larger than 10 GeV/c. The total number of muon hits of the muon track must be 45 or larger. To further ensure high-quality reconstructed tracks, the track in the event must also be reconstructed as two split standalone-muon tracks, one in the upper and one in the lower part of the muon barrel, with more than 20 hits each.

Table 2 reports the list of the event selection requirements and, for each of them, the number of events passing the selection. The absolute and the relative efficiency, for data and Monte Carlo simulation is also reported.

The analysis relies on the correct identification of the muon charge, which is described by the probability of charge mis-identification, defined as the fraction of muon particles reconstructed with wrong electric charge. This quantity is determined from Monte Carlo simulation, comparing the “true” charge of the muon at the generator level with the reconstructed one. The result is shown in Fig. 7 (top left), as a function of p_T^{PCA} for all the standalone-muon events, and for the sub-sample of events with an associated track present in the tracker detector. Results show that the probability of wrong charge assignment is smaller for the sample of standalone-muon tracks with associated tracker information. In the same figure the results for *tracker* tracks only are also shown. For such tracks the reconstructed muon charge is determined from tracker information only. The probability of charge mis-identification for such tracks is much smaller and well below 1% for any p_T^{PCA} value. Within the sample of standalone-muon tracks, approximately 30 % of the events also have tracks reconstructed in the tracker detector. From such events it is possible to measure the charge mis-identification probability by comparing the charge assigned to the standalone-muon track with the one of the tracker track, whose charge

Table 2: The event selection cuts of the standalone-muon analysis, with absolute and relative efficiencies for each sequential event selection cut in data and simulation. The efficiencies in simulation are shown as a reference, and do not play a direct role in the analysis. Differences between data and simulation are due to a momentum threshold at low momentum in the simulation, and known differences in the molasses model used in the MC samples leading to a differences in angular and momentum distributions.

selection	data			MC		
	N	ϵ (%)	rel. ϵ (%)	N	ϵ (%)	rel. ϵ (%)
exactly one standalone track	7604780	100	–	1173890	100	–
no CSC hit on track	7315293	96.2	96.2	1099080	93.6	93.6
track $p_T^{PCA} > 10$ GeV/c	4388403	57.7	59.9	768813	65.5	69.9
track $\phi < 0$	4382374	57.6	99.9	768231	65.4	99.9
track $N_{\text{hits}} > 45$	3854776	50.7	87.9	736932	62.8	95.9
exactly two split tracks	3677263	48.3	95.4	712412	60.7	96.7
split track in top and bottom	3651652	48.0	99.3	708492	60.4	99.5
split track $N_{\text{hits}} > 20$	3151343	41.4	86.3	646438	55.1	91.2

229 is shown to be correctly assigned with very high probability. Results for data and MC events
 230 are shown in Fig. 7 (top right) as a function of the muon transverse momentum p_T^{PCA} , measured
 231 at the PCA.

Similarly, the muon momentum scale and resolution are determined comparing the recon-
 232 structed transverse momentum p_T^{SA} and p_T^{Tk} assigned to the standalone-muon track and to
 233 the associated tracker track respectively. The transverse momentum is computed at the PCA in
 234 both cases. The quantity

$$\frac{\frac{1}{p_T^{SA}} - \frac{1}{p_T^{Tk}}}{\frac{1}{p_T^{Tk}}} \quad (2)$$

232 is computed for each transverse momentum interval, and fitted to a Gaussian function. The
 233 mean value of the Gaussian is defined as the momentum scale, whereas the σ is the momen-
 234 tum resolution. Figure 7 shows, on the bottom left, the momentum scale for data and for sim-
 235 ulated events. The bottom right plot displays the momentum resolution. Whereas the charge
 236 misassignment at high momentum is underestimated by the Monte Carlo simulation, the momen-
 237 tum scale and resolution are very well modelled. Therefore the momentum unfolding,
 238 which allows the determination of the true momentum of the muon tracks from the measured
 239 one, can be based on the Monte Carlo simulation, described in Section 4. The discrepancy in
 240 charge mis-assignment is important for this analysis, and a separate correction is applied. This
 241 is described in Section 5.

242 The measured muon charge ratio R , defined as the ratio of the observed number of positive to
 243 negative charged muons, is measured in intervals of p_T^{PCA} . The quantity R is shown in Fig. 6 as
 244 a function of p_T^{PCA} , with its statistical uncertainty.

245 Figure 8 shows the quantity R as a function of the distance of the PCA of the track to the CMS
 246 center, in the $x - y$ plane. Results for the standalone-muon tracks and, when available, also for
 247 the *tracker* tracks that are associated to the standalone-muon tracks are shown.

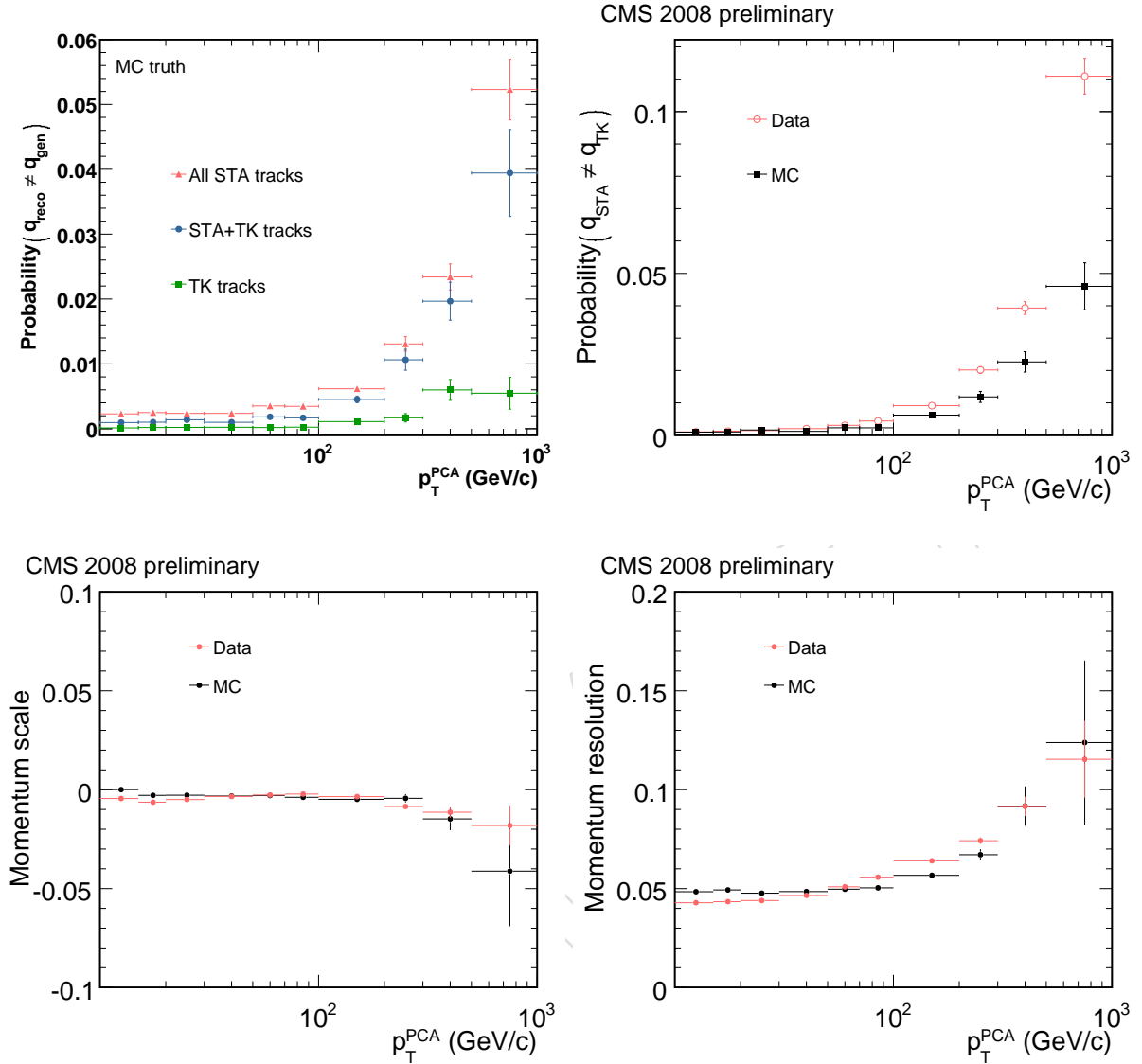


Figure 7: (Top left) True charge mis-assignment probability in simulated events, both for the whole standalone-muon sample and for standalone-muons with an associated *tracker* track. The charge assigned to the reconstructed track is compared with the “Monte Carlo truth” charge. (Top right) Charge mis-assignment probability as a function of the muon transverse momentum measured at the PCA, for data and simulated events. Results are determined from the comparison of the charge assigned to the reconstructed standalone muon to the *tracker* muon. (Bottom left and right) Momentum scale and resolution of the standalone-muon tracks in data and MC, obtained by comparing the reconstructed standalone-muon track to the *tracker* track (see text).

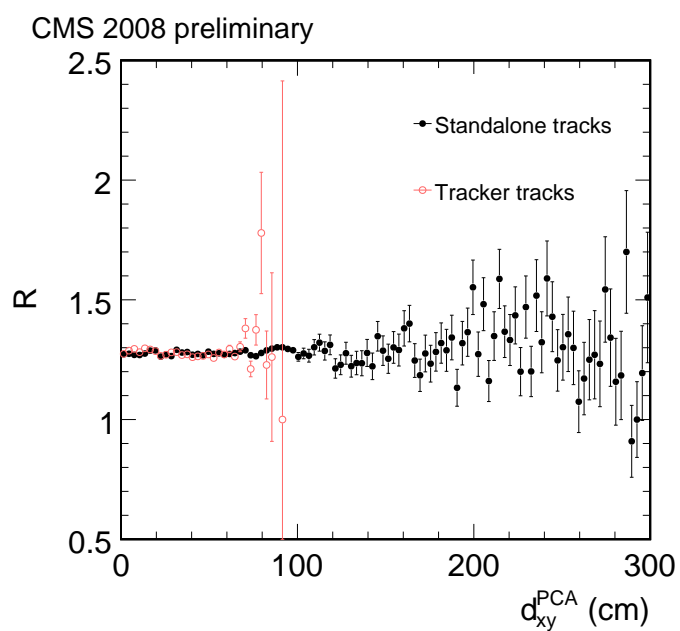


Figure 8: Uncorrected charge ratio R as a function of the distance of the PCA of the track to the center of CMS, in the $x - y$ plane, for the standalone-muon analysis. Results for the standalone-muon tracks and corresponding *tracker* tracks in (a subset of) the events are superimposed.

248 3.3 MTCC analysis

249 The cosmic muon charge ratio was measured by CMS for the first time using MTCC data and
250 is described in detail elsewhere [8].

251 For this analysis only part of the bottom sector of the barrel muon system was used. Special care
252 was taken to accept only muons triggered and reconstructed in a perfectly left-right symmetric
253 fiducial volume, ensuring a charge symmetric acceptance. The setup of the DT chambers is
254 depicted in Fig. 9 (left), together with the left-right symmetric fiducial acceptance.

255 The signals deposited in the DT detector by cosmic muons of positive and negative charge are
256 displayed in Fig. 9 (right), showing a symmetric illumination of the chambers, a key ingredient
of this fully data-driven analysis.

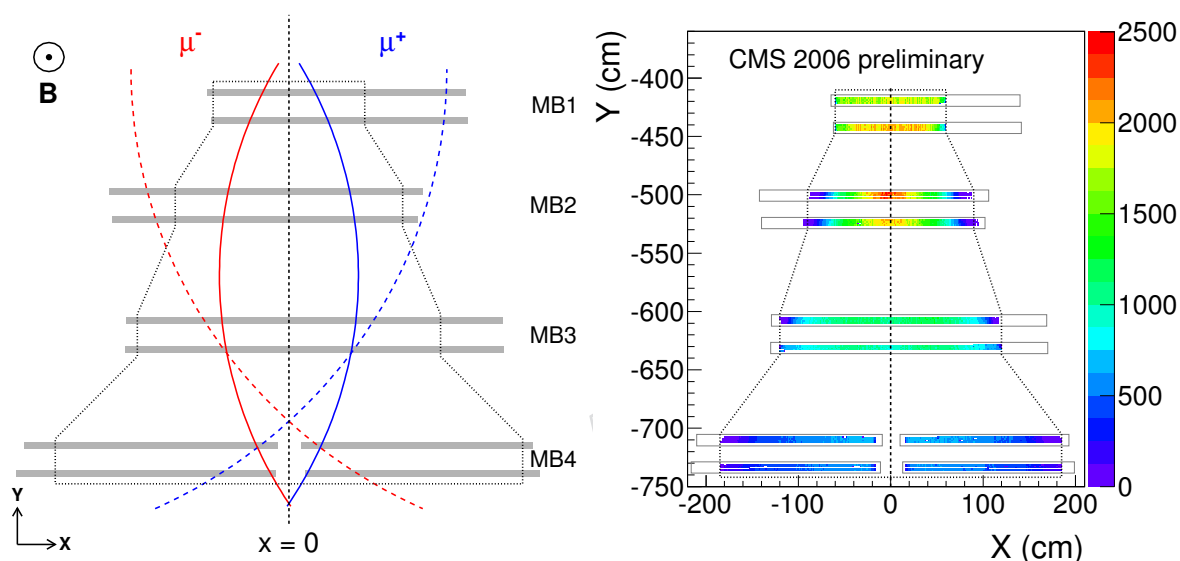


Figure 9: (Left) Definition of the left-right symmetric fiducial geometry (black dotted polygonal line) in the muon system. The dashed lines depict two muon tracks with the same momentum crossing the detector, the negative one satisfying the trigger condition requiring hits in the 2nd (MB2) and 3rd (MB3) muon station, and the positive one failing it. The solid curves represent two muons with the same p in the fiducial geometry, both of them passing the golden muon selection criteria. (Right) Distribution of hits in global XY coordinates, for muons of the MTCC run 4406 in wheel YB+1, after selection cuts are applied.

257

258 Around 15 million events were recorded in “good” runs with at least the DT chambers and DT
259 triggers included and a stable magnetic field above 3.67 T. A sample of about 330 thousand
260 events passes the selection cuts (both fiducial and track quality ones) [8]. The measured muon
261 charge ratio and its statistical uncertainty are displayed in Fig. 10, as function of the measured
262 muon momentum, before any correction due to detector effects is applied.

263 4 Extrapolation of raw measurements to the Earth surface

264 The ultimate goal of this measurement is to report the ratio of positive to negative muons, in
265 bins of true momentum, at the surface of the Earth. Thus the measured momentum inside the
266 CMS detector has to be corrected for energy lost between the surface of the Earth and the point
267 of measurement. Furthermore, corrections need to be applied for net momentum migration

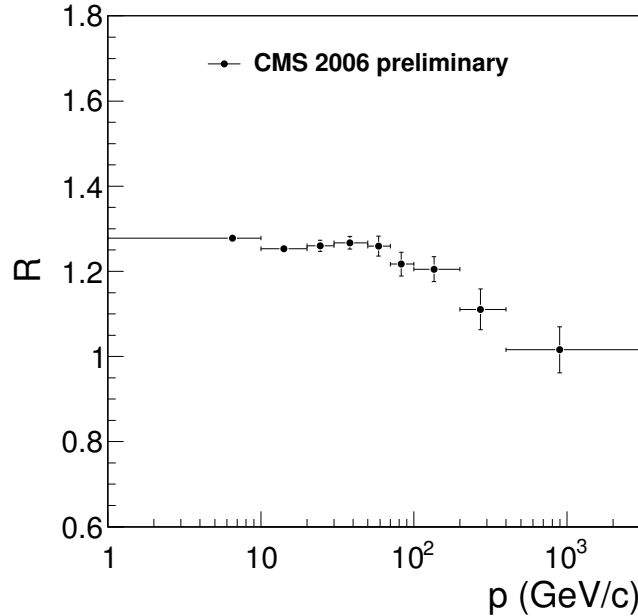


Figure 10: Cosmic muon charge ratio measured with MTCC data, as function of the measured muon momentum, before any correction due to detector effects is applied, together with the statistical uncertainty.

268 due to momentum resolution (on a steeply falling spectrum) and possible mis-assignment of
 269 the muon charge.

270 4.1 Correcting the CRAFT measurements for energy loss in the Earth

271 The same model used in the simulation (cf. section 2.2), is used to propagate the trajectory
 272 of each individual muon in CRAFT data back to the Earth surface, correcting for the average
 273 expected energy loss. It is assumed that energy loss is the same for muons of both charges. Ran-
 274 dom variations in energy loss are taken into account separately as an additional contribution
 275 to the momentum resolution, in the momentum unfolding procedure (see section 4.2.3).

276 Energy losses between the Earth surface (p^{Earth}) and the surface of CMS show large variation
 277 depending on the path followed through the Earth. Figure 11 depicts the estimated average
 278 energy loss for the muons selected in the global analysis.

279 4.2 Unfolding the momentum spectrum

280 To correct for momentum resolution effects in the detector, a natural variable to use is the
 281 curvature of the muon track in the magnetic field $C \propto q/p_T$. In this analysis we want to correct
 282 not only for the experimental resolution, but also for possible momentum migration due to
 283 imprecision in the correction for energy loss in the Earth.

284 We found that the best place to unfold for overall experimental momentum resolution effects
 285 is at the Earth surface, where the correlation between the *true* momentum and the *measured*
 286 momentum, extrapolated to the Earth surface, is highest. Since at high momentum the tracking
 287 resolution is still the dominant effect contributing to the momentum and charge determination,
 288 we found that the imaginary “curvature” defined as $C = q/p$ is still a natural variable to use at
 289 Earth surface, even though muon trajectories are straight in the absence of a strong magnetic
 290 field.

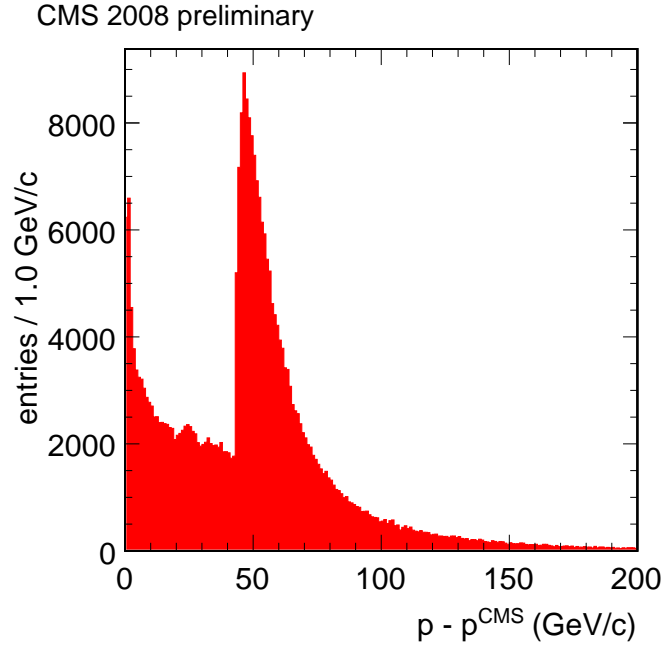


Figure 11: E_{loss} during propagation through the Earth.

291 We use a matrix inversion method to extract the true “curvature” $C^{true} = q/p^{true}$ of the muons
 292 at the surface of the Earth. The measured momentum, extrapolated to the surface of the Earth,
 293 gives us $C^{measured}$. Before describing how the true and the measured curvatures are constructed
 294 for the standalone and global analyses, we see that the unfolding can be done in a single matrix
 295 inversion,

$$C_i^{measured} = \sum_j M_{ij} C_j^{true} \quad (3)$$

$$C_i^{true} = \sum_j M_{ij}^{-1} C_j^{measured}$$

with M being the migration matrix, where M_{ij} is the number of times that we have observed a measured curvature in bin i , when the true curvature belonged to bin j . For the matrix inversion method to work, the migration matrix should have a spill-over (fraction per-column outside of the diagonal elements) smaller than 30%. We have found, as later will be shown, that the momentum bins below satisfy such condition.

$$p^{Earth} = (30, 50, 70, 100, 200, 400, \infty) \text{ GeV/c} \quad (4)$$

296 4.2.1 Global-muon analysis details

297 In the global muon analysis, the migration matrix is constructed using only the data.

298 To construct the migration matrix, two objects which will represent the “true” and “measured”
 299 curvatures are needed. The matrix should describe the effect of smearing by the resolution
 300 for a muon of a given curvature, which is represented by the half-difference d_C , as listed in

Equation 1. This will be achieved if the migration matrix elements are filled such that the true value is estimated by the curvature half-sum, and the measured value is the true value \pm the curvature half-difference d_C . Interestingly, these linear combinations give us the top and bottom curvatures,

$$C^{true} = \frac{1}{2} (C_{top} + C_{bottom})$$

$$C^{measured} = C^{true} \pm d_C = C_{top,bottom} \quad (5)$$

The curvatures $C_{top,bottom}$ at the Earth surface are the result of propagating the original (top and bottom) curvatures at the PCA, first to the top of CMS, accounting for the traversed amount of material and the magnetic field, by using the standard muon propagator, and second from the top of CMS to the surface of the Earth, following a straight line, as no magnetic field modifies the muon trajectory. We also measure the charge ratio as a function of $p \cos \theta_z$, with θ_z the zenith angle of the cosmic muons at the surface of the Earth, therefore we report both migration matrices (for p and $p \cos \theta_z$), already corrected for the energy loss spread as described in Section 4.2.3, in Figure 12. In both cases the spill-over is below 10%.

4.2.2 Standalone muon analysis details

Almost exactly the same procedure is used for the Standalone analysis. The only difference is that the migration matrix is extracted by comparing 'true' to reconstructed momentum in Monte Carlo simulation.

The distribution of the muon momentum determined at the earth surface, after the tracks are propagated backwards from the CMS detector, are unfolded by the smearing introduced by the momentum resolution, as described in Eq. 3. In Monte Carlo events the measured charge and momentum of the muon tracks, extrapolated to the earth surface, are unfolded and linked to the "true" charge and momentum via an unfolding matrix M , which is determined from simulation. The spill-over is always below 20 %. As for the global analysis, the matrix unfolding corrects both for momentum migration and charge mis-identification, on a statistical basis.

4.2.3 Energy loss spread in the Earth

While the average expected muon energy loss is uniquely defined by its path through the material and the incident muon momentum, random variations ("straggling") in the energy loss around the expected value occur. We found that the energy loss spread can be approximated as a Gaussian distribution around the expected value, with a sigma of approximately 10% of the energy loss.

This additional smearing of the momentum is applied to the measured momentum when forming the unfolding matrix. In the case of the stand-alone muon analysis this compensates for the fact that straggling is not included in the simulation. For the global muon analysis it takes into account the 10% uncertainty on the energy loss correction to be applied to the measured momentum in data.

In reality the energy loss variations are not Gaussian. For a small fraction of muons the energy loss can be (much) larger. This tends to move a small fraction of muons towards lower measured energy, where thanks to the steeply falling energy spectrum this background is negligible for the charge ratio measurement.

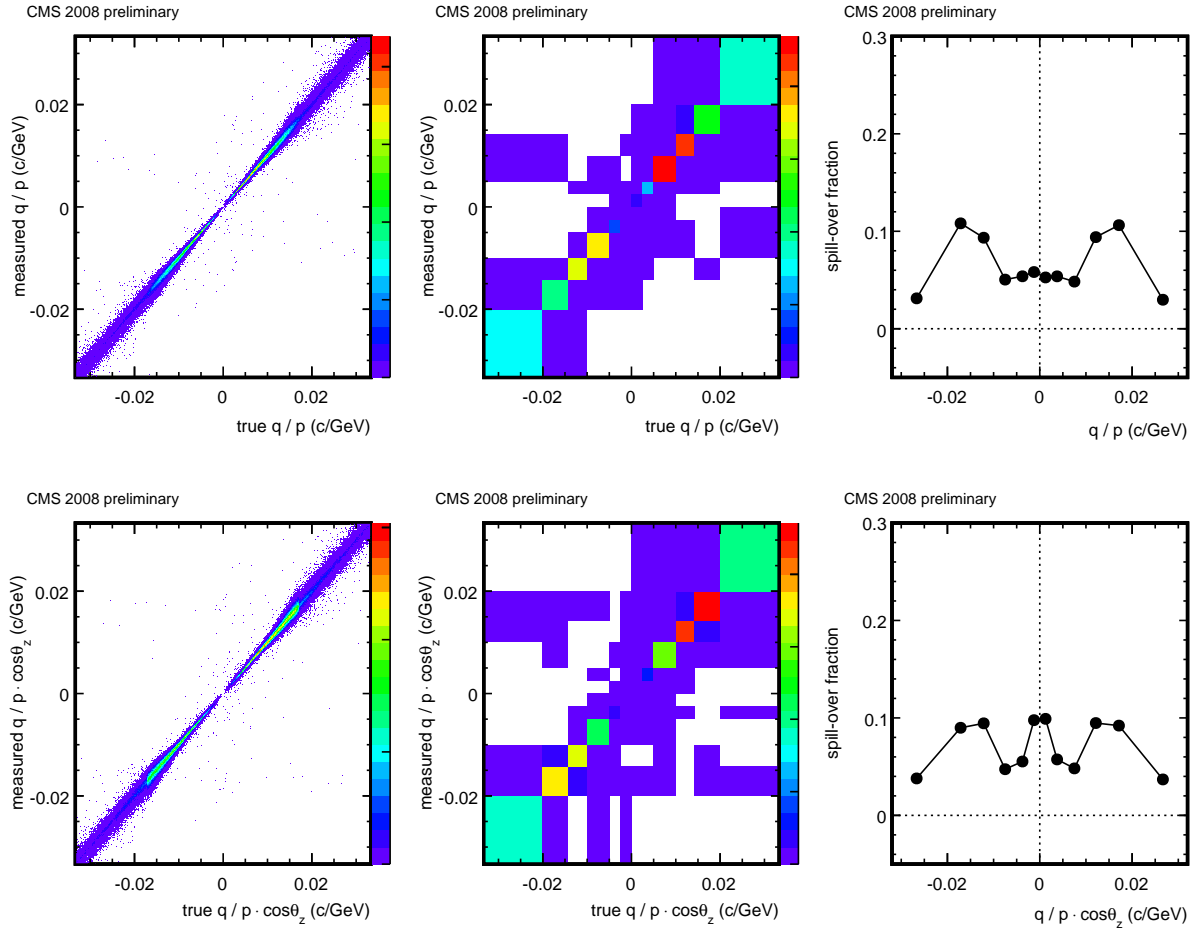


Figure 12: Global analysis migration matrices which transform even counts in bins of true q/p at the surface of the Earth to event counts in bins of measured q/p at the surface of the Earth (top). (Left) Fine binning for illustration. (Center) Actual binning. (Right) Off-diagonal spill-over by column. (bottom) The same plots for the corresponding migration matrix binned as function of $1/(p \cdot \cos \theta_z)$.

339 4.3 Results after propagation to the surface and unfolding

340 The measurement of the muon charge ratio in the stand-alone muon analysis, as a function of
 341 the momentum of the incident muon at the earth surface is reported in Fig. 13 (left). The results
 342 are also reported in Fig. 13 (right) as a function of p_y , the muon momentum component per-
 343 pendicular to the earth surface. Figure 14 displays similar graphs for the global-muon analysis.
 344

345 4.4 Energy loss correction in the MTCC analysis

346 In the MTCC analysis the measured muons are propagated back to the top of CMS, correcting
 347 for average momentum loss and bending in the magnetic field. In addition, the effect of charge
 348 confusion was estimated using Monte Carlo simulation and a bin-by-bin correction applied
 349 to the measured charge ratio. The measurement of the charge ratio using MTCC data as a
 350 function of the true muon momentum and its vertical component, along with the statistical and
 351 systematic uncertainties, is depicted in Fig. 15. Systematic uncertainties in the MTCC analysis
 352 are discussed in section 5.9.

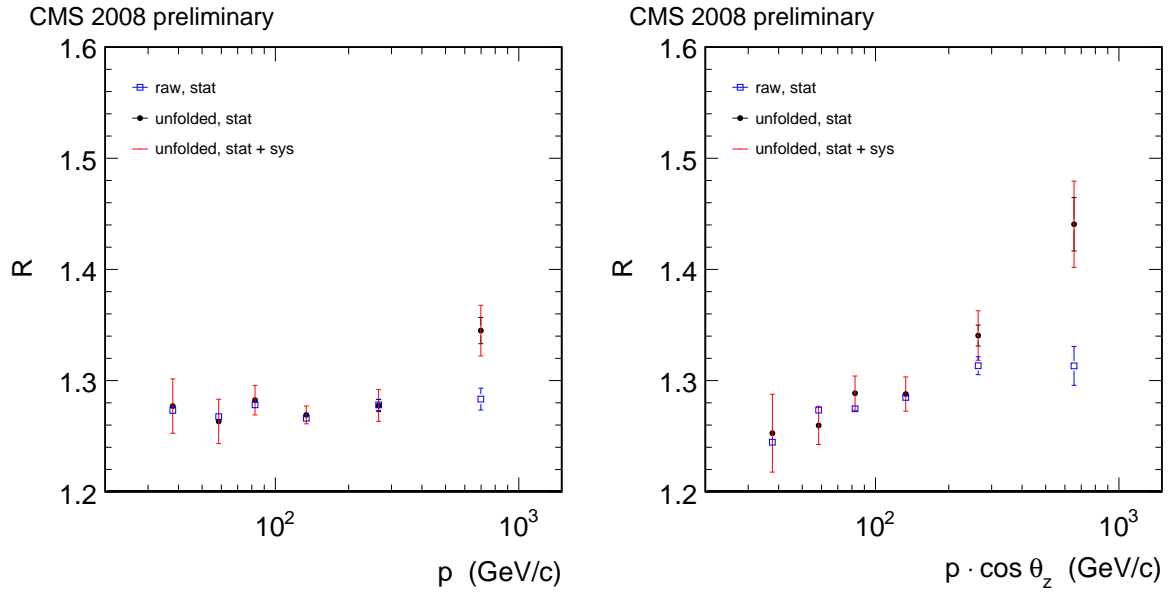


Figure 13: (Left) Muon charge ratio as a function of the muon momentum at the earth surface, for the standalone-muon analysis. (Right) Muon charge ratio as a function of the component of the muon momentum perpendicular to the earth surface. Statistical and systematic uncertainties are indicated by the error bars.

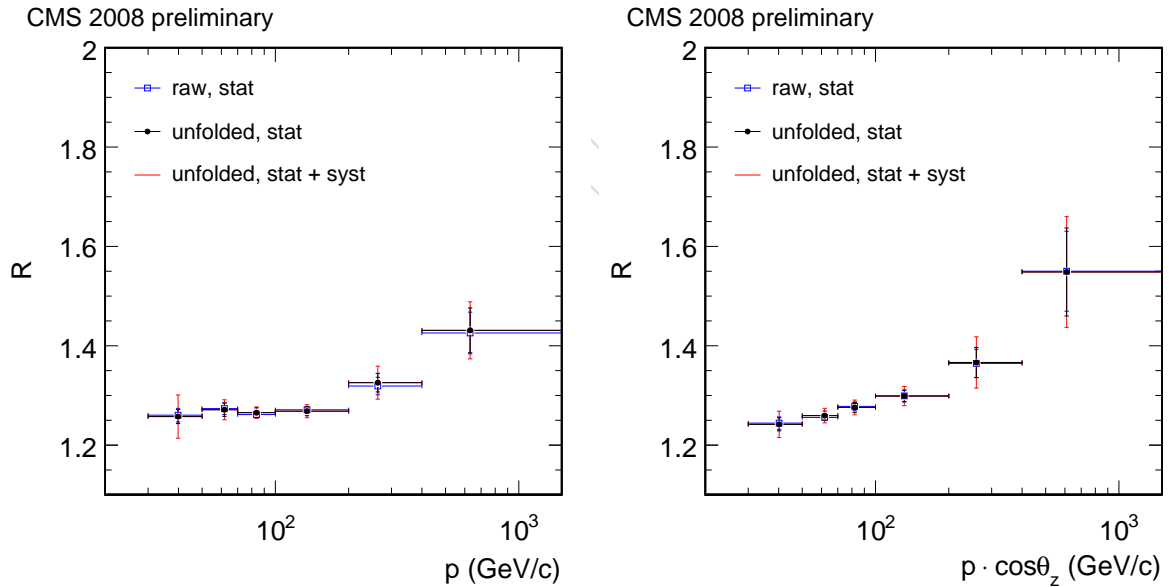


Figure 14: Muon charge ratio as a function of the muon momentum at the Earth surface (left) and vertical component of the momentum (right), for the global-muon analysis. (Blue open squares) The uncorrected ratio. (Black solid circles) Unfolded charge ratio, statistical error only. (Red lines) Statistical and systematic uncertainties combined.

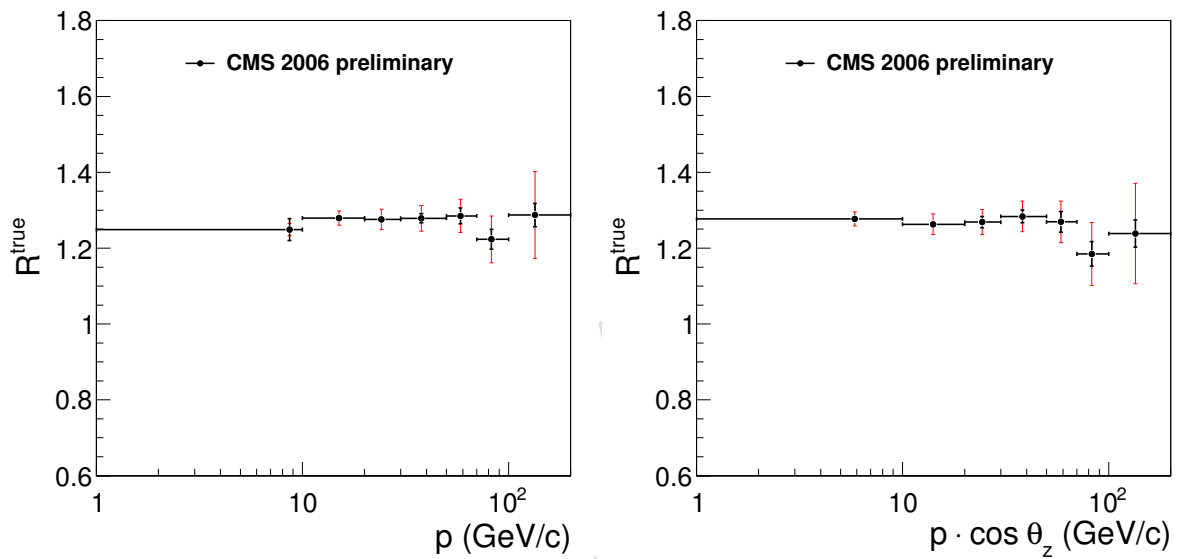


Figure 15: Charge ratio, as a function of the (left) muon momentum and (right) its vertical component, corrected for energy loss in the detector and for charge confusion, after propagating the muon track to the entry point in CMS. The thick black error bars denote the statistical uncertainty and the thin red ones the systematic.

5 Systematic uncertainties

Systematic uncertainties for the cosmic muon charge ratio are evaluated in each p and $p \cos \theta$ bin, at the surface of the Earth. In most cases the systematic uncertainties are estimated as the quadratic sum of the observed bias plus the statistical uncertainty of the deviation. In this section we described the different sources of systematic effects considered. The corresponding estimated systematic effects are summarized in Table 3.

5.1 Event selection

To estimate the systematic uncertainty introduced by the event selection, the effect of each cut on the measured charge ratio is determined by excluding that cut from the event selection, and comparing the obtained charge ratio with the reference one. The difference between the two results is assigned as a systematic uncertainty for the selection cut under study. No statistically significant effect was found.

5.2 Magnetic field

Any uncertainty in the description of the magnetic field has an impact on the interpretation of the measured curvature of the muon tracks. The momentum measurement and possibly even their assigned charge could be affected. Dedicated studies were performed on CRAFT data leading to an accurate knowledge of the magnetic field [16]. To estimate a residual systematic uncertainty, a comparison between the results from the data reconstructed with the latest magnetic field map, and with an older version, which still provided a rather good description of the magnetic field, is performed. The difference between the two results is assigned as a systematic error. No statistically significant effect was found.

5.3 Alignment

The global alignment between the tracker and muon systems is key to reconstructing high- p_T muons, in the context of global muon reconstruction - poor alignment will lead to wrong charge assignments and p_T migrations. The effects of alignment are different for the standalone muon reconstruction, where only the relative alignment and orientation of DT muon chambers plays a role. To estimate this systematic bias in the global-muon analysis, we re-fit the muon track fits in every event with different misalignment scenarios applied on the MC sample. It should be noted that due to the different nature of the effect of alignment on the standalone and the global muon fit, this systematic effect is not expected to be highly correlated between the two analyses.

5.4 Trigger

Both analyses estimate the systematic bias induced by the trigger employing a tag-and-probe technique. In the case of the global analysis, we can study the trigger bias by requiring one of the legs caused the trigger ("tag") and studying the bias on the other leg, when it also caused a trigger ("probe"). We study the trigger efficiency separately for positive and negative muons, and assign a systematic uncertainty based on how much the ratio of the two efficiencies disagrees with unity. In the case of the standalone analysis, the sample is selected either by the DT or by the RPC muon trigger. The charge bias introduced by the DT trigger is estimated selecting a sample of events triggered by the RPC, and measuring how the positive to negative muon ratio is affected by the DT selection. In a similar way the bias of the RPC trigger is also determined, selecting a sample of DT triggered events. The DT and RPC triggers are found to be uncorrelated. A small ($<1\%$) but significant effect is observed at low momentum, and is

396 quoted as a systematic uncertainty. This systematic error is expected to be correlated between
397 the analyses.

398 **5.5 Charge mis-assignment**

399 This systematic uncertainty is only considered for the standalone analysis. In the global anal-
400 ysis the effect of charge mis-assignment is small to begin with, and it is corrected for by the
401 data-driven resolution estimator defined in Equation 1.

402 The measured muon charge ratio (Fig. 8 (left)) is corrected taking into account the probability
403 of the muon charge misassignment as a function of the muon momentum. This procedure is
404 included in the unfolding matrix. The charge misassignment is determined from Monte Carlo
405 simulation, comparing the “true” and the reconstructed charge of the *standalone* muon candi-
406 dates, for the various momentum intervals. The reliability of the Monte Carlo prediction on the
407 charge misassignment was tested in real data using the sub-sample of *standalone* muons with
408 an associated tracker track. In this sub-sample of events a systematic difference in the prob-
409 ability of charge misassignment is observed between data and simulation (Fig. 7 (top right)).
410 This difference is applied as a correction to the charge misidentification probability determined
411 from Monte Carlo, and a systematic uncertainty equal to 50 % of the correction is assigned.

412 However, this correction is strictly valid only for the sub-sample of *standalone* muons with
413 an associated tracker track, and not for the whole *standalone* sample. Therefore the observed
414 difference, in Monte Carlo events, between the charge misidentification probability determined
415 over the whole *standalone* sample and over the *tracker* sub-sample (Fig. 7 (top left)) is assigned
416 as an additional systematic uncertainty.

417 **5.6 Material model**

418 The molasses above CMS are composed of about 50 m moraines and 22 m rock. The relative
419 uncertainty in the density of each component is $\sim 5\%$. Then, to estimate the material model
420 systematic, for both standalone and global analyses we compare the results obtained when
421 the propagation to the Earth surface in data is performed with two different sets of material
422 densities. The difference between the two results is assigned as the systematic error. To first
423 order no effect on the charge ratio is expected, since muons of both charges are affected equally.

424 **5.7 Muon losses**

425 Cosmic muons can be absorbed on their way from the Earth surface to the center of CMS.
426 Depending on their incident angle and energy, the muon losses vary with the original (true)
427 momentum at the Earth surface. In any case, we find no specific reason other than the access
428 shafts to affect in different ways positive and negative muons, combined with the fact that
429 muons of opposite charge bend in opposite direction in the detector, leading to a slightly dif-
430 ferent angular distribution of detected muons. In this situation, low momentum muons will be
431 the most affected by these losses, as they can only reach the CMS detector by crossing the Earth
432 through the access shafts, and they bend more in the CMS detector. Accordingly, it is natural
433 to expect this effect to decrease with increasing momentum.

434 We use Monte Carlo simulation to compare the generated muon spectrum with the sample of
435 muons reaching CMS and passing all analysis cuts, thus estimating the overall efficiency as a
436 function of the generated muon momentum. We are interested in the ratio of this efficiency
437 for positively and negatively charged muons. Only in the lowest momentum bin (30 GeV/c –
438 50 GeV/c) a statistically significant bias is observed, and assigned as a systematic uncertainty

439 for that bin. No significant effect is observed in the remaining muon spectrum, and the other
 440 bins are combined to yield a single number to be quoted in table 3.

441 5.8 Unfolding procedure

442 The last question to be answered is if the chosen unfolding procedure introduces any bias in the
 443 final result. As we don't have access to the true migration matrix, we have derived an estimator
 444 using MC. Then, with an ensemble of 500 toy MC experiments, we check the deviation of the
 445 unfolded results from the true input by looking at the pulls distributions, for each momentum
 446 bin. We find no noticeable deviation, and therefore no systematic uncertainty is assigned to the
 447 unfolding procedure.

448 5.9 Summary

449 The breakdown of the various systematic uncertainties is reported in Figures 16 and 17, for both
 450 p and $p \cos \theta$ at the Earth surface. All the global and standalone analyses relative systematic
 uncertainties are summarized in Table 3, for both p and $p \cos \theta_z$.

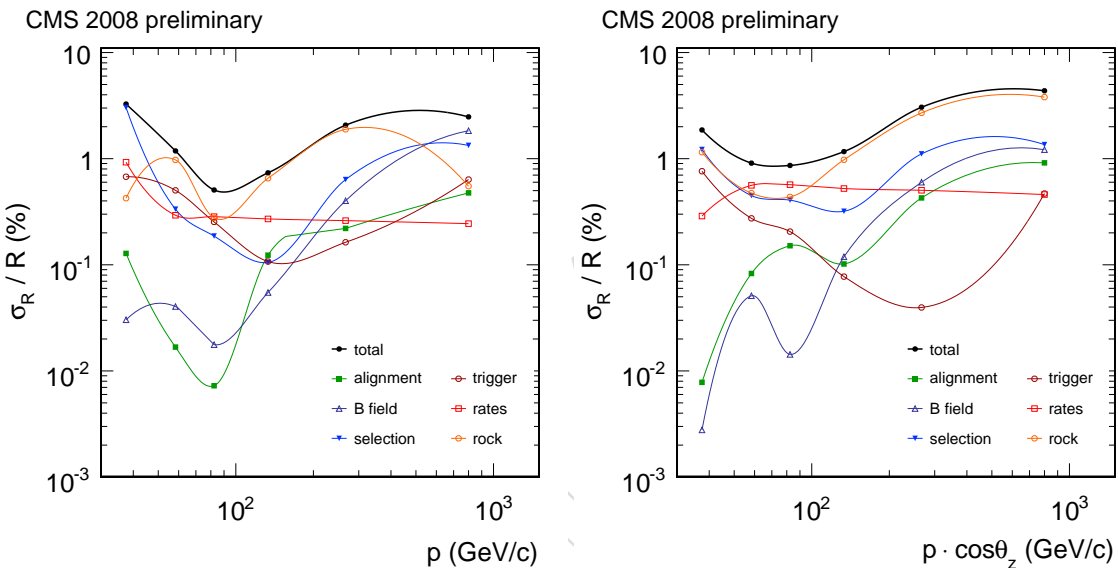


Figure 16: Relative systematic uncertainties of the global analysis vs. p (left) and $p \cos \theta$ (right) at the Earth surface.

451

452 In the MTCC analysis, systematic uncertainties arise mainly from finite precision of the detec-
 453 tor alignment parameters, from the correction of the charge mis-assignment probability (given
 454 by detector resolution) and from a slightly larger uncertainty ($\sim 5\%$) on the magnetic field scale.
 455 The contribution of the various sources of systematic uncertainty are depicted in Fig. 18, to-
 456 gether with the total systematic uncertainty, as a function of the muon momentum and its
 457 vertical component. The relative systematic uncertainties are summarized in Table 4, both for
 458 p and $p \cos \theta_z$.

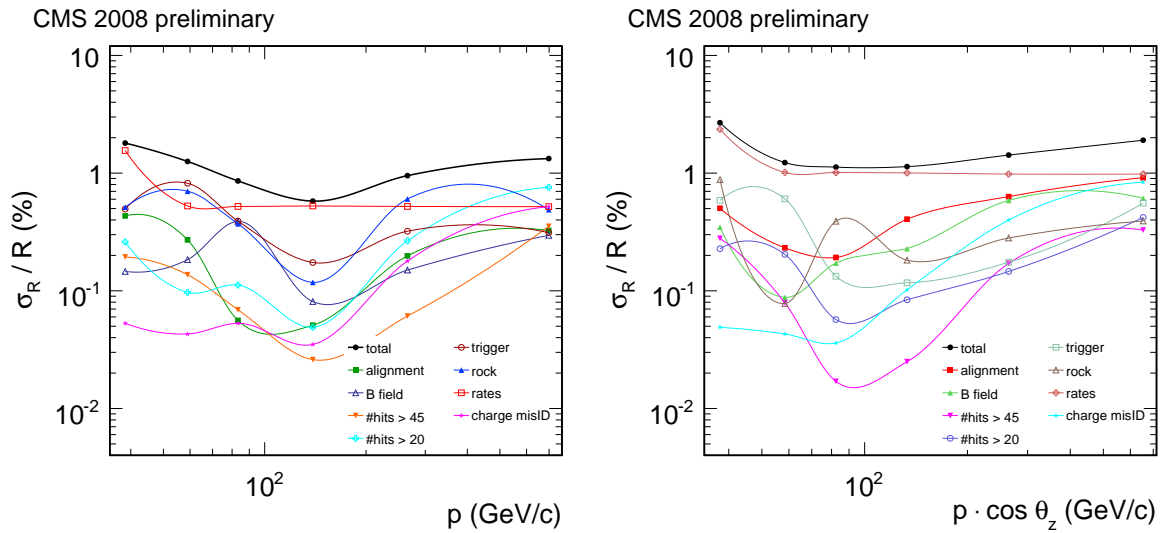


Figure 17: Relative systematic uncertainties of the standalone analysis vs. p (left) and $p \cos \theta$ (right) at the Earth surface.

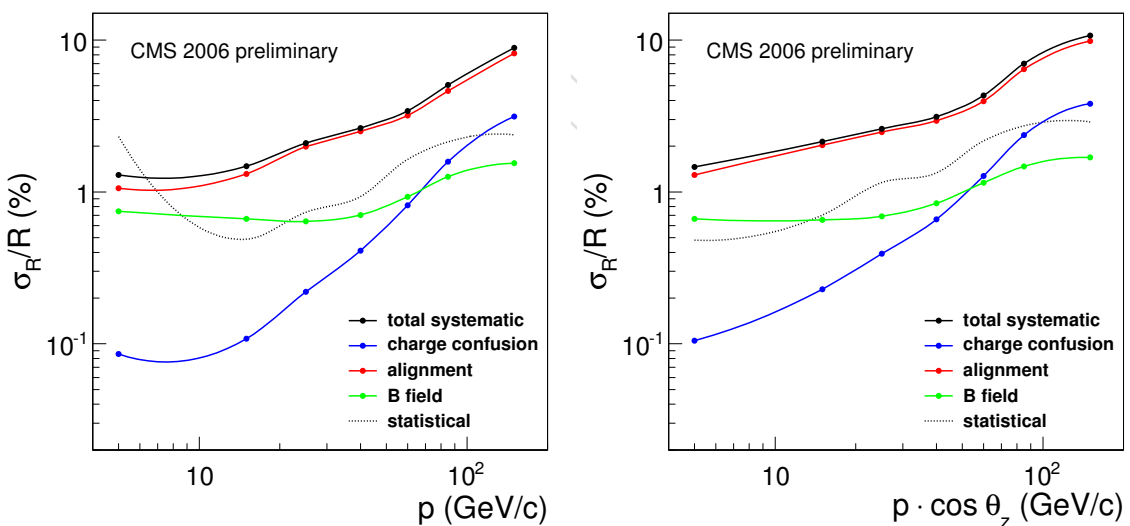


Figure 18: Relative systematic uncertainty in the MTCC analysis, together with the contribution of the various sources, as function of (left) the muon momentum and (right) the vertical component of the muon momentum. The statistical uncertainty is also displayed.

Table 3: Relative systematic uncertainties as a function of p and $p \cos \theta_z$ for the global and standalone fits.

p range (GeV/c)	R	global σ/R (%)																			
		stat.	syst.	DT	SL2	TOB	χ^2	alignment	B field	trigger	rates	rock	1-leg	2-leg	ch. mis.	alignment	B field	trigger	rates	rock	
30 - 50	1.257	1.13	3.27	-2.36	0.81	1.65	-0.51	-0.13	0.03	-0.68	0.93	0.42									
50 - 70	1.271	1.05	1.18	-0.08	-0.03	0.30	-0.11	-0.02	-0.04	-0.50	-0.29	0.97									
70 - 100	1.265	0.76	0.51	-0.02	-0.15	0.10	-0.03	-0.01	-0.02	-0.25	-0.28	0.28									
100 - 200	1.268	0.72	0.74	0.00	-0.06	-0.07	0.06	-0.12	-0.05	-0.11	-0.27	-0.65									
200 - 400	1.326	1.41	2.07	0.20	-0.00	-0.16	-0.58	0.22	0.40	0.16	-0.26	-1.89									
400 - ∞	1.431	3.15	2.48	-0.86	0.14	-0.55	-0.85	-0.48	-1.83	0.64	-0.24	0.55									
$p \cos \theta_z$ range (GeV/c)	R	global σ/R (%)																			
		stat.	syst.	DT	SL2	TOB	χ^2	alignment	B field	trigger	rates	rock	1-leg	2-leg	ch. mis.	alignment	B field	trigger	rates	rock	
30 - 50	1.242	1.05	1.86	-0.19	0.55	1.02	-0.34	-0.01	-0.00	0.76	0.29	1.15									
50 - 70	1.259	0.72	0.91	-0.43	-0.09	0.02	-0.08	-0.08	-0.05	0.27	-0.56	-0.47									
70 - 100	1.276	0.78	0.86	0.38	-0.08	0.06	0.09	-0.15	0.01	0.21	-0.57	-0.44									
100 - 200	1.299	0.92	1.17	0.15	-0.11	0.07	-0.25	0.10	0.12	0.08	-0.52	-0.98									
200 - 400	1.366	2.22	3.05	0.53	-0.03	-0.02	-0.97	0.43	-0.60	0.04	-0.50	-2.70									
400 - ∞	1.549	5.72	4.36	-1.28	0.40	0.03	-0.22	0.91	-1.22	-0.47	-0.46	3.80									
p range (GeV/c)	R	standalone σ/R (%)																			
		stat.	syst.	1-leg	2-leg	ch. mis.	alignment	B field	trigger	rates	rock	1-leg	2-leg	ch. mis.	alignment	B field	trigger	rates	rock		
30 - 50	1.277	0.3	1.6	-0.03	0.08	0.05	0.01	0.10	-0.47	1.41	-0.51										
50 - 70	1.263	0.3	1.3	-0.03	-0.07	0.04	0.07	-0.16	-0.65	-0.30	0.70										
70 - 100	1.282	0.2	0.8	-0.02	-0.06	0.05	0.10	0.38	-0.27	-0.30	-0.36										
100 - 200	1.269	0.2	0.3	-0.02	0.06	0.04	0.02	-0.03	-0.12	-0.30	-0.08										
200 - 400	1.278	0.5	0.8	-0.03	-0.12	0.20	-0.04	-0.05	0.18	-0.30	0.58										
400 - ∞	1.345	0.9	1.1	-0.09	-0.26	0.91	-0.05	-0.11	0.02	-0.29	0.40										
$p \cos \theta_z$ range (GeV/c)	R	standalone σ/R (%)																			
		stat.	syst.	1-leg	2-leg	ch. mis.	alignment	B field	trigger	rates	rock	1-leg	2-leg	ch. mis.	alignment	B field	trigger	rates	rock		
30 - 50	1.253	0.3	2.6	-0.03	0.07	0.05	0.05	0.33	-0.54	2.27	0.88										
50 - 70	1.260	0.2	1.0	-0.02	-0.05	0.04	0.03	0.06	-0.47	-0.86	-0.03										
70 - 100	1.289	0.2	1.0	0.02	-0.06	0.04	0.07	0.15	-0.09	-0.85	0.38										
100 - 200	1.288	0.3	0.9	-0.02	-0.08	0.11	0.03	-0.21	-0.07	-0.85	0.15										
200 - 400	1.341	0.7	1.5	-0.05	-0.18	0.11	-0.85	-0.54	0.01	-0.83	0.19										
400 - ∞	1.441	1.7	2.1	-0.16	-0.42	1.83	0.27	0.39	-0.33	-0.83	-0.13										

Table 4: Relative systematic uncertainties as a function of p and $p \cdot \cos \theta_z$ for the MTCC analysis.

p range (GeV/c)	R	σ/R (%)					B field
		stat.	syst.	ch. mis.	alignment		
5 - 10	1.2490	2.31	1.30	0.09	1.06	-0.75	
10 - 20	1.2793	0.49	1.48	0.11	1.32	0.66	
20 - 30	1.2756	0.74	2.10	0.22	1.99	-0.64	
30 - 50	1.2787	0.93	2.63	0.41	-2.50	0.70	
50 - 70	1.2849	1.64	3.42	0.82	-3.19	-0.91	
70 - 100	1.2232	2.14	5.06	1.58	-4.63	-1.29	
100 - 200	1.2874	2.38	8.89	3.14	-8.18	-1.54	
$p \cdot \cos \theta_z$ range (GeV/c)	R	σ/R (%)					B field
		stat.	syst.	ch. mis.	alignment		
2 - 10	1.2771	0.48	1.46	0.10	1.29	-0.66	
10 - 20	1.2629	0.70	2.15	0.23	2.03	0.65	
20 - 30	1.2686	1.15	2.61	0.39	2.48	-0.70	
30 - 50	1.2837	1.33	3.13	0.66	-2.94	0.82	
50 - 70	1.2693	2.17	4.31	1.27	-3.95	-1.15	
70 - 100	1.1848	2.72	7.01	2.37	-6.42	-1.49	
100 - 200	1.2384	2.89	10.69	3.81	-9.85	-1.69	

6 Results

The results from the three analyses are shown in Figure 19. In momentum bins where the different analyses overlap the agreement between them is good, and we average them to obtain a combined result in each bin. To do this, we assume zero correlations between different sources of systematic effects. The combined data points are given in Table 5, and shown in Fig. 19. Data points are placed at the bin average, determined in a fit to simulation, with the standalone (STA) and global (GLB) points offset by $\pm 5\%$ for clarity.

Table 5: The muon charge ratio R from the combination of all three CMS analyses.

p (GeV/c)	$\langle p \rangle$ (GeV/c)	R	Stat. error	Sys. Error
0-10	5.47	1.249	0.029	0.033
10-20	13.7	1.279	0.006	0.020
20-30	24.2	1.276	0.009	0.028
30-50	37.8	1.275	0.004	0.017
50-70	58.5	1.268	0.006	0.013
70-100	82.5	1.274	0.005	0.008
100-200	134.0	1.269	0.003	0.004
200-400	265.8	1.284	0.006	0.011
>400	689.0	1.354	0.012	0.018
$p \cdot \cos \theta_z$ (GeV/c)	$\langle p \cdot \cos \theta_z \rangle$ (GeV/c)	R	Stat. error	Sys. Error
0-10	5.33	1.277	0.006	0.020
10-20	13.6	1.263	0.009	0.029
20-30	24.1	1.269	0.015	0.036
30-50	37.7	1.254	0.007	0.019
50-70	58.4	1.260	0.004	0.010
70-100	82.4	1.282	0.005	0.010
100-200	133.1	1.291	0.004	0.010
200-400	264.0	1.345	0.009	0.020
>400	654.0	1.453	0.024	0.037

6.1 Interpretation

Models of cosmic ray showers indicate the detected muons originate in decays of pions and kaons. Based on the quark content of protons in the atmosphere, and the observation that primary cosmic ray particles are mostly positive, the ratio of π^+ / π^- is predicted to be around 1.27 [17]. Due to the phenomena of associated production, the charge ratio of strange particles such as kaons is expected to be even higher.

The expected muon spectrum has been parameterized [18] based on the kinematics of primary cosmic ray particles and of decays of secondary particles, and from this parameterization, the charge ratio can be extracted [5], with the form:

$$r_\mu = \frac{\frac{f_\pi}{1+1.1E_\mu \cos \theta_z / 115 \text{ GeV}} + \frac{\eta \cdot f_K}{1+1.1E_\mu \cos \theta_z / 850 \text{ GeV}}}{\frac{1-f_\pi}{1+1.1E_\mu \cos \theta_z / 115 \text{ GeV}} + \frac{\eta \cdot (1-f_K)}{1+1.1E_\mu \cos \theta_z / 850 \text{ GeV}}} \quad (6)$$

where f_π and f_K are the fractions of all pion and kaon decays that yield positive muons. The constant η sets the relative pion and kaon fraction on cosmic ray showers, and we take the accepted value of 0.054 [18]. Based on the height of the atmosphere and particle lifetimes,

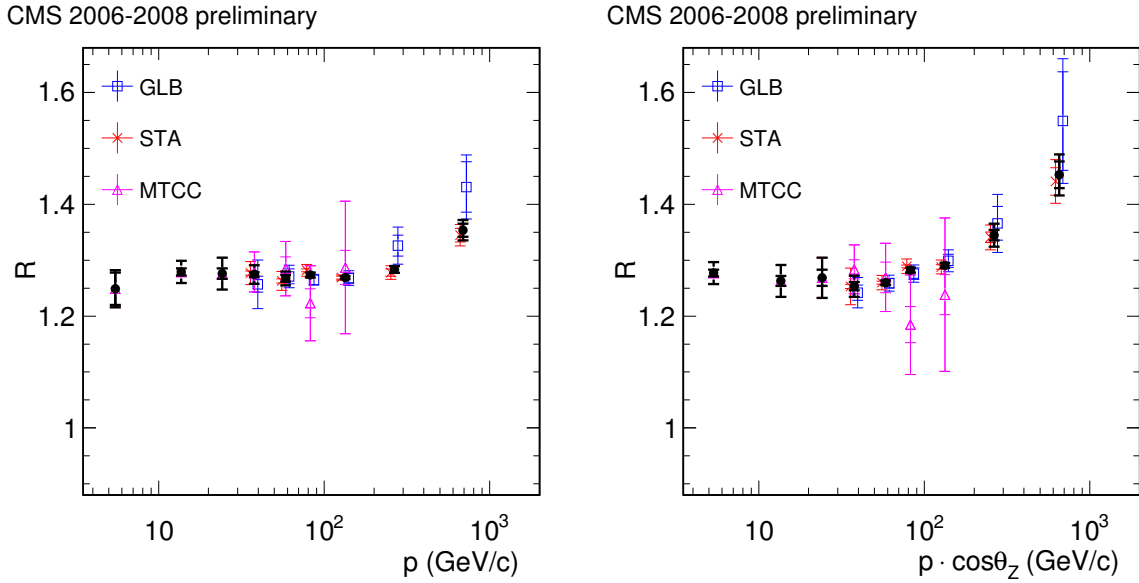


Figure 19: The three CMS results, and their combination, (left) as a function of the muon momentum and (right) of its vertical component.

475 115 GeV and 850 GeV are the energies above which a pion or kaon has a lower than 50% prob-
 476 ability to have decayed before reaching the earth. Based on this charge ratio is expected to rise
 477 significantly in the region 115 GeV – 850 GeV, as the proportion of muons from kaon decays
 478 increases.

479 We therefore extract two values from the data: the charge ratio in the region $p \cdot \cos\theta_z <$
 480 100 GeV, where it is expected to be flat; and a fit to the entire measured region, to determine f_π
 481 and f_K .

482 6.2 Charge ratio below 100 GeV

483 In the region $p \cdot \cos\theta_z < 100$ GeV, we have measurements in six $p \cdot \cos\theta_z$ bins. Three bins are
 484 covered from all three analyses, with the surface-based MTCC analysis extending the reach
 485 to three lower momentum bins. We combine these 12 data points into a single measurement
 486 of the charge ratio using a standard prescription [19], with the following scenario for correla-
 487 tions: each individual systematic source for each analysis is correlated across all all bins for
 488 that analysis; further, the “trigger”, “rates” and “rock” systematics are correlated between the
 489 STA and GLB analyses. This yields a charge ratio of $1.2769 \pm 0.0025(stat) \pm 0.0025(syst)$, with
 490 a $\chi^2/d.o.f. = 2.7$. This in good agreement with the most precise published measurement in
 491 this region, performed by the L3+C collaboration: $1.285 \pm 0.003(stat) \pm 0.019(syst)$ [4], and it
 492 also represents a significant improvement in precision. Indeed, the uncertainty in each of the
 493 5 $p \cdot \cos\theta_z$ bins reported here is of comparable accuracy to the combined uncertainty of the
 494 previous measurement. However, the high $\chi^2/d.o.f.$ indicates the data are in this region are
 495 not consistent with a flat charge ratio. Fitting just the region below 80 GeV yields a charge ratio
 496 of $1.2652 \pm 0.0028(stat) \pm 0.0035(syst)$ with a $\chi^2/d.o.f. = 0.61$, more consistent with the flat
 497 charge ratio hypothesis.

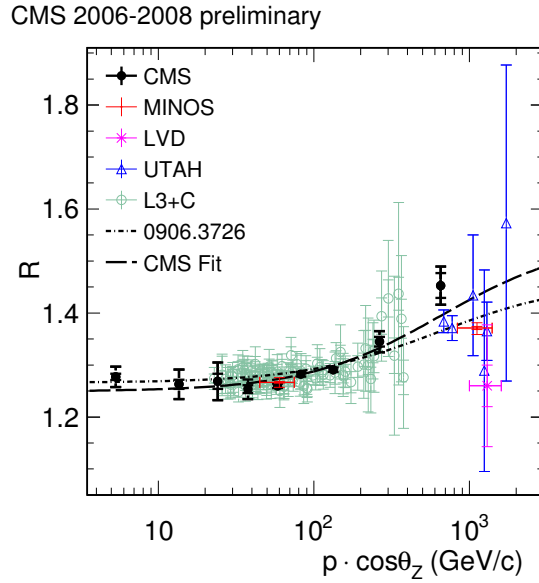


Figure 20: The CMS fit, along with previous measurements and a fit to those measurements.

498 6.3 Extracting f_π and f_K

499 The resulting measurements are then fitted using Equation 6 to extract f_π and f_K . In performing
 500 this fit, we use the same scenario for correlating the systematics within each analysis, and
 501 between the STA and GLB analyses. We measure $f_\pi = 0.5442^{+0.0040}_{-0.0035}$, and $f_K = 0.762^{+0.040}_{-0.045}$,
 502 with a $\chi^2/d.o.f. = 2.2$, suggesting some of the simplifying assumptions used in this model
 503 are insufficient to describe the data. A combination of previous measurements yielded $f_\pi =$
 504 0.5510 ± 0.0006 , and $f_K = 0.7006 \pm 0.0061$ [5]. Figure 20 shows the fit to CMS data only, along
 505 with this previous fit and the data used therein. However we note that the f_π value is largely
 506 driven by the L3+C data below 100 GeV, and the precision obtained by this fit suggests that a
 507 1.5% correlated systematic uncertainty between the L3+C data points was not fully accounted
 508 for, artificially lowering the uncertainty on f_π from about 1% to about 0.1% in this previous
 509 combination.

510 In summary, we have presented the most precise measurement to date of the charge ratio in
 511 the region $p \cdot \cos \theta_z < 100$ GeV, and in the critical region 115 GeV–850 GeV.

512 7 Conclusions

513 We have measured the ratio of positive- to negative-charge cosmic muons, as a function of the
 514 muon momentum and its vertical component, using data collected by the CMS experiment at
 515 the *Magnet Test and Cosmic Challenge* (MTCC) and at the *Cosmic Run At Four Tesla* (CRAFT08).
 516 The analysis has been performed in an environment identical to that designed for the analysis
 517 of the data coming from pp collisions at LHC, using standard CMS reconstruction software,
 518 data distribution and job submission tools. While physics studies were not among the goals of
 519 the cosmic runs, we have succeeded to obtain a result of good quality, which is in agreement
 520 with previous measurements within the experimental uncertainties. This is the first measure-
 521 ment of a physical quantity performed with muons by the CMS experiment.

References

- 522
- 523 [1] CMS Collaboration, "The CMS Experiment at the CERN LHC", *JINST* **0803**: (2008) 08004.
524 doi:10.1088/1748-0221/2/08/S08004.
- 525 [2] J. Evans and B. P., "LHC Machine", *JINST* **3** (2008) 08004.
526 doi:10.1088/1748-0221/3/08/S08001.
- 527 [3] CMS Collaboration, CMS Physics Technical Design Report, Volume II: Physics
528 Performance, *J. Phys. G: Nucl. Part. Phys.* **34** (2007) 995-1579.
- 529 [4] T. Hebbeker, C. Timmermans, *Astropart. Phys.* **18** (2002) 107-127;
530 J.M. Baxendale, C.J. Hume, M.G. Thompson, *J. Phys. G* **1** (1975) 781-788;
531 B.C. Rastin, *J. Phys. G* **10** (1984) 1629-1638;
532 P. Achard et al., L3 Collaboration, *Phys. Lett. B* **598** (2004) 15-32.
- 533 [5] P. A. Schreiner, J. Reichenbacher, and M. C. Goodman, "Interpretation of the
534 Underground Muon Charge Ratio", arXiv:0906.3726v1.
- 535 [6] CMS Collaboration, The CMS Magnet Test and Cosmic Challenge (MTCC Phase I and II)
536 Operational Experience and Lessons Learnt, CMS-NOTE 2007/005.
- 537 [7] CMS Collaboration, "Commissioning of the CMS Experiment and the Cosmic Run at
538 Four Tesla", arXiv:0911.4845v1.
- 539 [8] M. Aldaya and P. Garcia-Abia, "Measurement of the charge ratio of cosmic muons using
540 CMS data", *CMS Note* **2008/016** (2008).
- 541 [9] Ph. Biallass, Th. Hebbeker, Parametrization of the Cosmic Muon Flux for the Generator
542 CMSCGEN, arXiv:0907.5514v1 [astro-ph.IM].
- 543 [10] L. Sonnenschein, Cosmic muons in simulation and measured data, Conference Report
544 CMS CR-2010/005 (Lepton Photon 09).
- 545 [11] D. Heck et al., CORSIKA, A Monte Carlo to simulate Extensive Air Showers,
546 Forschungszentrum Karlsruhe, Report FZKA 6019 (1998).
- 547 [12] Particle Data Group, Review of particle physics, p. 230, *Phys. Lett. B*, **592**, 1-4 (2004).
- 548 [13] CMS Collaboration, CMS Muon Technical Design Report, CERN/LHCC 1997-032.
- 549 [14] CMS Collaboration, CMS Tracker Technical Design Report, CERN/LHCC 1998-006.
- 550 [15] CMS Collaboration, "Performance of CMS Muon Reconstruction in Cosmic-Ray Events",
551 arXiv:0911.4994v2.
- 552 [16] CMS Collaboration, "Precise Mapping of the Magnetic Field in the CMS Barrel Yoke
553 using Cosmic", arXiv:0910.5530.
- 554 [17] G. Fiorentini, V.A. Naumov and F.L. Billante, *Phys. Lett. B* **510**, 173 (2001).
- 555 [18] T. Gaisser, *Cosmic Rays and Particle Physics*, Cambridge University Press, 1990.
- 556 [19] L. Demortier, R. Hughes, R. Roser, Averaging the Top Quark Mass Measurements from
557 CDF and D0, CDF/ANAL/TOP/CDFR/4439, Version 2.5 (1998); L. Lyons, D. Gibaut, P.
558 Clifford, How to Combine Correlated Estimates of a Single Physical Quantity, *Nucl.*
559 *Instrum. Meth. A* **270** (1988) 110; A. Valassi, Combining correlated measurements of
560 several different physical quantities, *Nucl. Instrum. Meth. A* **500** (2003) 391.

561 A Supporting documentation

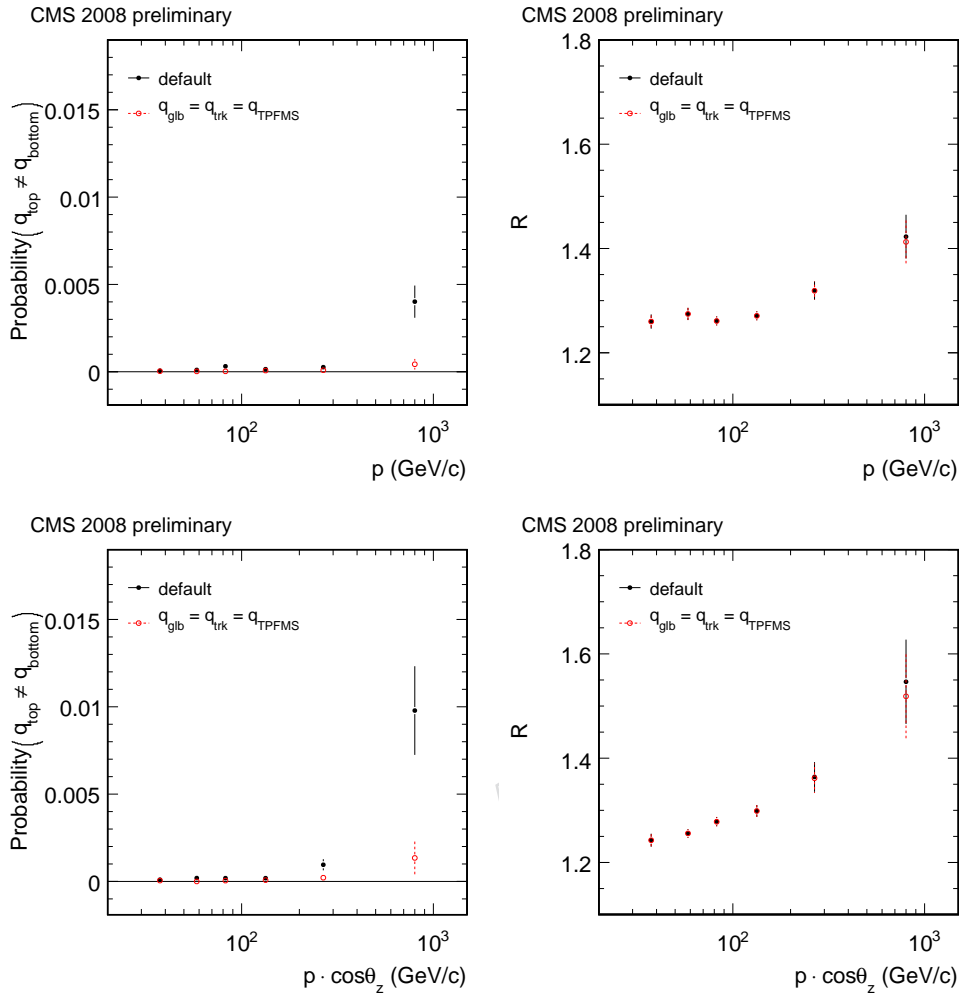


Figure 21: (Left) Measured rate of charge mis-assignment. (Right) Measured charge ratio. (Top) As a function of p at the Earth surface. (Bottom) As a function of $p \cos \theta$ at the Earth surface. The black solid circles depict the default results. The red open circles show the effect of requiring the same charge for three different algorithms (global, tracker and TPFMS [15]), separately for the top and bottom hemispheres. This consistency requirement has a high efficiency (99.9% on the overall sample, down to 97.9% in the highest p bin, and 96.5% in the highest $p \cos \theta$ bin) but it reduces charge misassignment considerably. While not used by default in this analysis, the above plots are a powerful cross-check, demonstrating that the effect of charge confusion on the measured charged ratio is minimal in the whole momentum range considered.

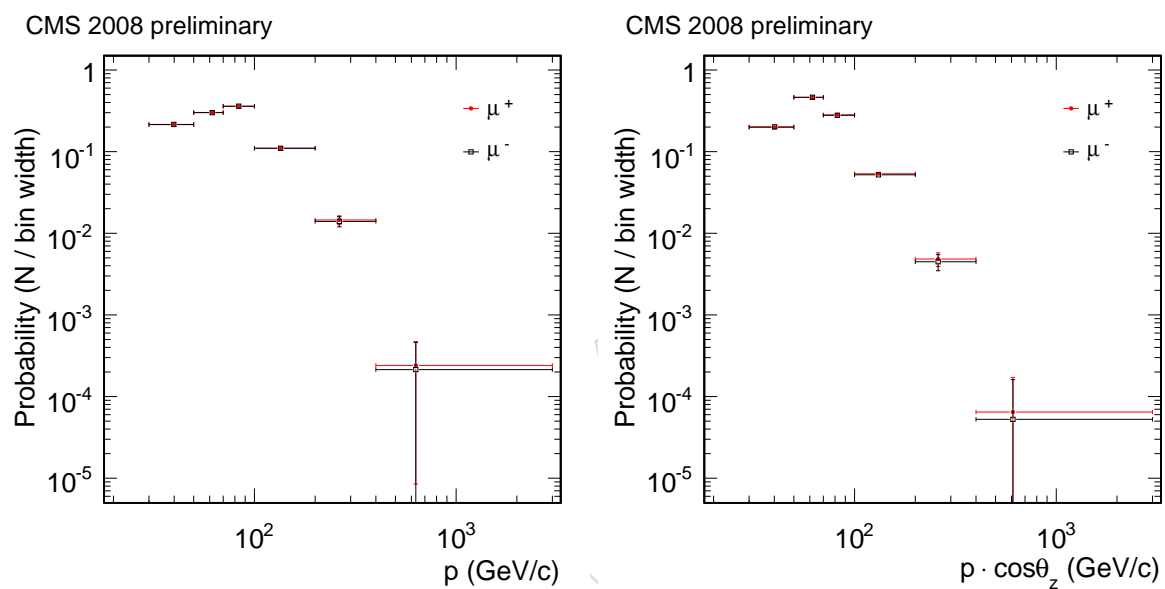


Figure 22: Global analysis measured p (left) and $p \cos \theta$ (right) at the Earth surface. Positive (red solid circles) and negative (black open squares) muon distributions are normalized to the same area.